Advances in Water Resources 78 (2015) 94–111

Contents lists available at ScienceDirect

Advances in Water Resources

journal homepage: www.elsevier.com/locate/advwatres

Unraveling the hydrology of a Himalayan catchment through integration of high resolution in situ data and remote sensing with an advanced simulation model

S. Ragettli [a,*], F. Pellicciotti [a], W.W. Immerzeel [a,b], E.S. Miles [c], L. Petersen [a], M. Heynen [a], J.M. Shea [d], D. Stumm [d], S. Joshi [d], A. Shrestha [d]

[a] Institute of Environmental Engineering, ETH Zurich, Zurich, Switzerland
[b] Department of Physical Geography, Utrecht University, Utrecht, Netherlands
[c] Scott Polar Research Institute, University of Cambridge, Cambridge, UK
[d] International Centre for Integrated Mountain Development, Kathmandu, Nepal

ARTICLE INFO

Article history:
Received 8 May 2014
Received in revised form 2 December 2014
Accepted 25 January 2015
Available online 2 February 2015

Keywords:
Himalayas
Mountain hydrology
Debris covered glaciers
Glacier mass balance
In situ measurements
Runoff modeling

ABSTRACT

The hydrology of high-elevation watersheds of the Hindu Kush-Himalaya region (HKH) is poorly known. The correct representation of internal states and process dynamics in glacio-hydrological models can often not be verified due to missing in situ measurements. We use a new set of detailed ground data from the upper Langtang valley in Nepal to systematically guide a state-of-the art glacio-hydrological model through a parameter assigning process with the aim to understand the hydrology of the catchment and contribution of snow and ice processes to runoff. 14 parameters are directly calculated on the basis of local data, and 13 parameters are calibrated against 5 different datasets of in situ or remote sensing data. Spatial fields of debris thickness are reconstructed through a novel approach that employs data from an Unmanned Aerial Vehicle (UAV), energy balance modeling and statistical techniques. The model is validated against measured catchment runoff (Nash–Sutcliffe efficiency 0.87) and modeled snow cover is compared to Landsat snow cover. The advanced representation of processes allowed assessing the role played by avalanching for runoff for the first time for a Himalayan catchment (5% of annual water inputs to the hydrological system are due to snow redistribution) and to quantify the hydrological significance of sub-debris ice melt (9% of annual water inputs). Snowmelt is the most important contributor to total runoff during the hydrological year 2012/2013 (representing 40% of all sources), followed by rainfall (34%) and ice melt (26%). A sensitivity analysis is used to assess the efficiency of the monitoring network and identify the timing and location of field measurements that constrain model uncertainty. The methodology to set up a glacio-hydrological model in high-elevation regions presented in this study can be regarded as a benchmark for modelers in the HKH seeking to evaluate their calibration approach, their experimental setup and thus to reduce the predictive model uncertainty.

1. Introduction

The Hindu Kush-Himalaya region (HKH) holds the largest volume of ice outside the polar regions and thus stores important freshwater resources [36]. Climate change is expected to have significant consequences on snowmelt and glacier runoff across the region (e.g. [42,53]). Understanding the present hydrological regimes and climatological and glaciological processes of high-elevation catchments is thus vital. This requires better insights into the present composition of runoff and interactions between climate, glaciers, snow and soil.

Our knowledge of high-altitude snow/ice and its response to climate is still incomplete [10,16]. In the Himalayas, fieldwork is difficult due to the remoteness of glaciers as well as logistical, financial and political obstacles. For this reason, in recent years the focus has been on remote sensing approaches used to reconstruct snow cover, frontal and areal changes of glaciers and ice volumetric changes (e.g. [29,46,83]). However, in the light of possible changes in the snow- and glacier-energy balance due to climatic changes, there is a strong call for more in situ measurements across the Himalayas and models that integrate those data in space and time [10,16,77]. Local processes and effects

* Corresponding author at: ETH Zurich, Institute of Environmental Engineering, Stefano-Franscini-Platz 5, 8093 Zurich, Switzerland. Tel.: +41 44 633 27 30.
E-mail address: ragettli@ifu.baug.ethz.ch (S. Ragettli).

http://dx.doi.org/10.1016/j.advwatres.2015.01.013
0309-1708/

that are difficult to study using remotely sensed data could explain regional differences and temporal changes in glacier mass balance across the region, such as the glacier expansion in the central Karakorum known as the 'Karakorum anomaly' [33]. Recent studies on the spatial variability of glacier extension and mass balance across the HKH point at the importance of varying monsoon and westerly winds influence on the local climate [46,93], but also of gravitational redistribution of snow, glacier flow dynamics and the interplay between glacier surface characteristics such as debris cover and albedo, topography and energy fluxes reaching the glacier surface [34].

Glacio-hydrological models are indispensable tools to study these effects and to understand the characteristics of a catchment and its response to climate. They are however subject to a number of factors that complicate their applicability in high elevation regions: (i) the lack of representative data to force the models [37,67], (ii) simplifications in model structure due to insufficient process understanding and the scarcity of detailed information about glacio-hydrological processes [37] and (iii) parametric uncertainty due to insufficient quality or paucity of data for model calibration and validation (e.g. [75]). A growing number of studies have assessed the relation between snow- and/or glacier changes and runoff production at the catchment scale in the HKH using models (e.g. in the Central Himalaya: [41,42,48,49,59,70], or in the Karakorum: [9,66,75]). However, the applied models were calibrated using a maximum of two response variables (usually runoff and/or remotely sensed snow cover). Many studies have not included observations about the cryosphere other than initial glacier outlines (e.g. [59,70,75]). The use of only one or two response variables increases the risk that many combinations of parameters yield the same result, which leads to a large degree of predictive uncertainty [8]. Also, most previous modeling studies do not use meteorological data from stations above 4000 m asl – where most glaciers are. Finally, data scarcity is also the reason why the effect of variable debris thickness on glacier melt is rarely considered and why there is no previous modeling study in the HKH region which reproduces observed avalanche patterns.

The present study has two main goals. First, to provide high resolution (temporally and spatially) simulations of the full water balance of a high-elevation catchment in the HKH to improve our understanding of the role of cryospheric processes for streamflow generation. These simulations (i) incorporate high elevation data as model inputs, (ii) make use of state-of-the art algorithms to model the relevant processes, and (iii) use local data to constrain parametric uncertainty and limit equifinality problems. The second goal is to provide recommendations on network design and the timing and location of field measurements, in order to collect the data that can be most efficiently used to constrain the uncertainties of the glacio-hydrological model. For this purpose we developed an approach that assesses the capacity of model parameters and variables to explain uncertainty in a given model output [75]. For the present study this approach is also used to assess the effectiveness of ongoing monitoring programs within the study catchment, the upper Langtang catchment in Nepal.

This study presents thus a methodological framework to set up a glacio-hydrological model for a high-elevation Himalayan catchment. We make use of a unique set of ground data combined with high resolution satellite observations to inform our choice of model parameters. Through advanced high-resolution modeling we provide a fundamental understanding of the role of individual processes for streamflow generation in a Himalayan head-water catchment. The methodology enables a detailed assessment of the state of the glaciers within the catchment, their role in runoff production and the processes controlling their response to climate.

2. Study area and climate

This study focuses on the upper Langtang catchment, located approximately 50 km north of Kathmandu, Nepal (Fig. 1). The catchment has an area of 350 km^2, with a total glacier portion of 33.8%, of which 27% are debris covered. Only at the less steep slopes along the main river sparse forest and grassland exists (approximately 1.5% of the catchment area [48]). Boulders and scree cover the steep slopes and high plateaus. The outlet of the upper Langtang catchment is at 3650 m asl (Fig. 1a).

The tongues of the largest glaciers within the catchment are debris covered (Table 1). Field observations indicate that the composition of the debris layer is highly heterogeneous, from very fine silt to large boulders exceeding several meters in height. The largest glacier is Langtang Glacier, in the northeast of the catchment. The Lirung Glacier, with the greatest elevation range (4040–7180 m asl) has been the site of several glaciological investigations in the past [57,78–80]. Other glaciological studies focused on Yala Glacier, a non-debris covered glacier [1,4,22,24,25,88]. Glacierization and snow cover in the catchment have been documented by Iida et al. [38], Shiraiwa et al. [84] and Steinegger et al. [86] and more recently by Pellicciotti et al. [68].

The climate in the Langtang valley is monsoon dominated and approximately 70% of the annual precipitation falls during the monsoon (mid-June–September, [43]). Outside of this period precipitation is limited and is produced by the occasional passage of westerly troughs during post-monsoon (October–November) or winter (December–February). Localized convective precipitation events occur during the pre-monsoon (March–mid-June, [43]). Seasonally, temperatures are highest during the monsoon, with rising (falling) temperatures during the pre-monsoon (post-monsoon) periods.

3. Data and methods

The modeling approach presented in this study aims at making maximal use of in situ data for the estimation and calibration of model parameters. The instruments that have been installed since May 2012 and that provide data for this study are

- Two permanent automatic weather stations (AWSs) at Kyangjing (AWS K, 3862 m asl) and near Yala Glacier (AWS Y, 5090 m asl).
- A pluviometer and a sonic ranging sensor near Yala Glacier (Pluvio, 4831 m asl) [43].
- Two temporary AWSs on Lirung Glacier (AWS L-G, 4164 m asl) and on Yala Glacier (AWS Y-G, 5204 m asl).
- Tipping buckets and temperature sensors (T-Loggers) installed at various locations in the main valley [43].
- T-Loggers installed on Lirung Glacier.
- Stakes installed on Yala Glacier for mass balance observations [4].
- Newly equipped hydrological stations for runoff measurements at the outlet and near Lirung Glacier.

The characteristics and locations of the hydro-meteorological stations are provided in Table 2. Locations are shown in Fig. 1. Station data are complemented by data measured manually in the field (debris thickness, snow density, terminus position of Lirung Glacier). New rating curves were obtained in 2012 and 2013 for Langtang Khola (at the outlet of the upper Langtang catchment) and Lirung Khola (near Lirung Glacier) by tracer (constant-rate injection) and current meter measurements and coincident observations of stream height from an automated pressure level transducer at Lirung Khola and a radar water level sensor at Langtang

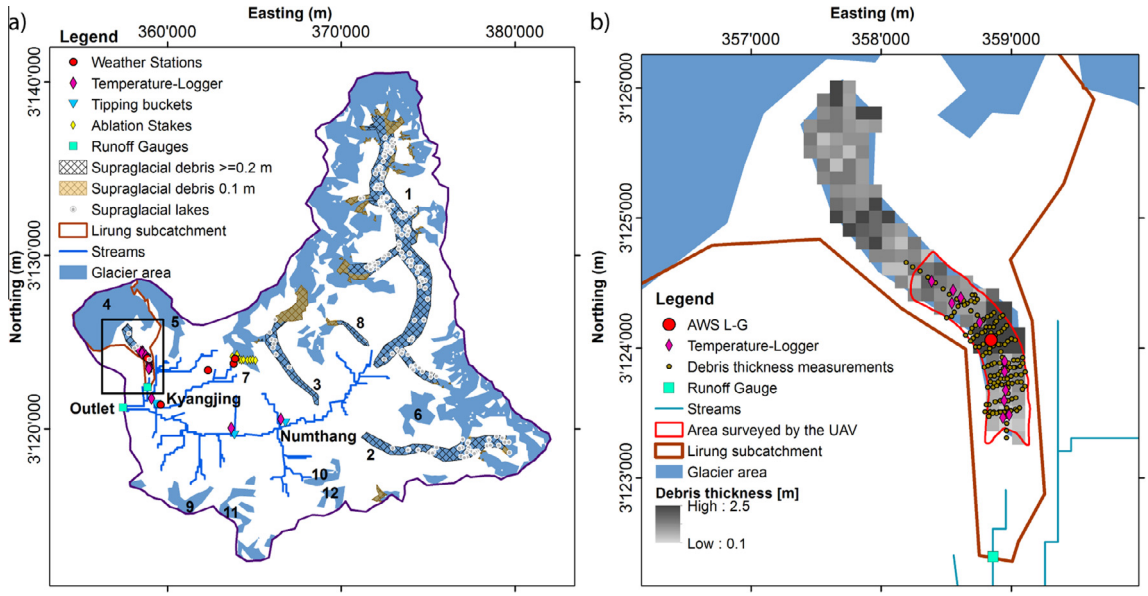

Fig. 1. (a) Map of the upper Langtang catchment showing the position of meteorological stations and streamgauges (Table 2), tipping buckets and temperature loggers, ablation stakes and Landsat ETM+ derived supraglacial lakes. The numbers on the map indicate the locations of glaciers listed in Table 1. (b) Map of the glacier tongue of Lirung Glacier. The Unmanned Aerial Survey System (UAV) range shows the area that has been mapped by airborne stereo imagery in May and October 2013. The debris thickness values within the UAV range indicate reconstructed debris thickness, and outside the UAV range the randomly sampled reconstructed debris thickness.

Table 1
Names and characteristics of glaciers within the upper Langtang valley.

Name	ID	Area [km^2]	Elevation range [m asl]	Mean elevation [m asl]	Debris cover (%)	Mean slope (%)	Main aspect [°]	Mass balance [m w.e./a]	AAR (%)	IC rank	IC rank elev. corrected
Langtang	1	57.1	4490–7160	5510	35	46	230	−0.13	55	9	12
Langshisha	2	16.8	4420–6840	5520	33	43	310	−0.21	50	7	10
Shalbachum	3	11.6	4210–6690	5380	37	49	147	−0.36	37	8	11
Lirung	4	11.3	4040–7180	5490	10	94	130	−0.80	22	6	3
Kimoshung	5	4.2	4400–6360	5610	0	39	215	0.69	83	10	6
Langshisha Ri	6	2.7	4970–6270	5770	0	47	191	0.52	78	12	7
Yala	7	1.6	5170–5630	5370	0	42	211	−0.17	44	3	5
Ghanna	8	1.4	4720–5860	5150	56	45	71	−0.57	24	5	9
Urkin Kangari	9	1.3	5110–5450	5300	0	23	11	−0.92	13	1	2
Gangchenpo 1	10	1.3	4990–5880	5450	0	46	292	0.58	56	4	4
Kanja La	11	1.2	5100–5830	5320	0	29	45	−0.71	28	2	1
Gangchenpo 2	12	1.1	5140–6300	5760	0	72	220	0.16	29	11	8

Only glaciers with an area larger than 1 km^2 are shown. Locations of glaciers are indicated in Fig. 1a. *Mass Balance*, Accumulation area ration (*AAR*) and information content (*IC*) ranks are modeling results that correspond to the model setup tested by case 8 (Table 4). *Slope* is the ratio between vertical and horizontal distance, *Aspect* is expressed clockwise from north.

Table 2
Characteristics and location of the hydro-meteorological stations used in this study.

Station	Code	Elevation (m asl)	Latitude	Longitude	Location	Period of functioning
AWS Kyangjing	AWS K	3862	28.2108	85.5695	Kyangjing village	01 May 2012–17 Nov 2013
AWS Lirung Glacier	AWS L-G	4164	28.2349	85.5613	Lirung Glacier tongue	13 May 2012–25 Oct 2012, 9 May 2013–23 Oct 2013
AWS Yala	AWS Y	5090	28.2325	85.6121	Close to Yala Glacier	01 May 2012–17 Nov 2013
AWS Yala Glacier	AWS Y-G	5204	28.2352	85.6127	Yala Glacier ablation area	7 Jun 2012–20 Jun 2012
Pluviometer Yala	Pluvio	4831	28.2290	85.5970	near Yala	08 May 2012–11 Jun 2013
Lirung Khola streamgauge	Lirung Q	3971	28.2199	85.5617	Outlet Lirung subcatchment	1 May 2013–17 Nov 2013
Langtang Khola streamgauge	Langtang Q	3652	28.2091	85.5475	Study catchment outlet	01 Apr 2012–17 Nov 2013

Khola. We also use remotely sensed data of snow cover (Landsat ETM+ and MODIS) and stereo imagery provided by an Unmanned Aerial Vehicle (UAV). Landsat ETM+ data were atmospherically-corrected via the LandCor implementation of the 6S radiative transfer model [50,94]. The UAV dataset is used to obtain high-resolution digital elevation models (DEMs) of Lirung Glacier that provide surface height changes and is described in detail in [40].

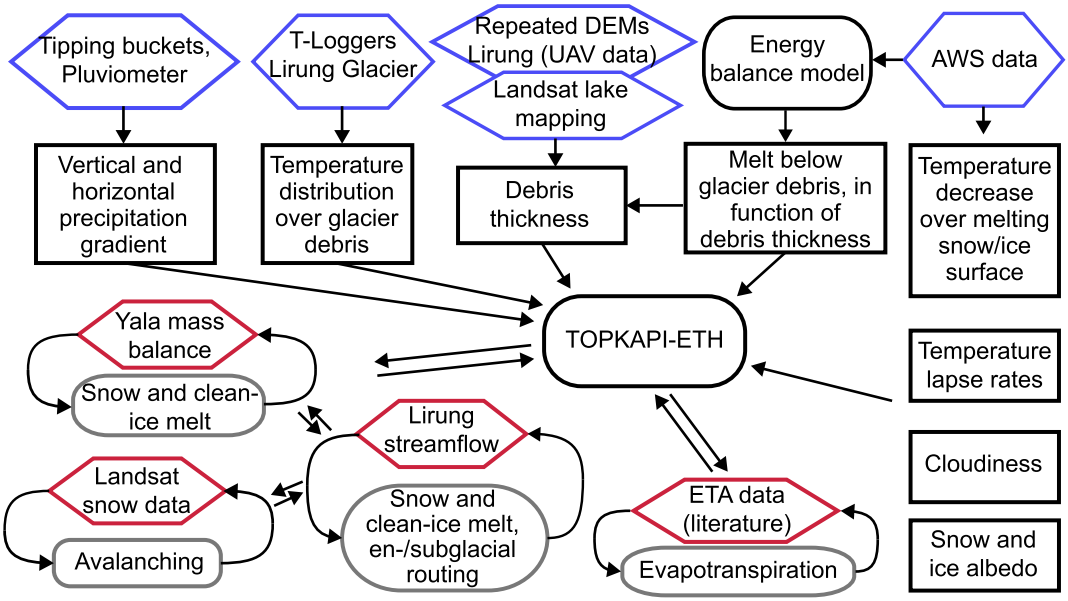

Fig. 2. Scheme of the methodology developed to estimate optimal model parameters for the upper Langtang valley making maximal use of available in situ data. Rectangular boxes represent model parameters that are directly calculated using local data (blue hexagons). Those parameters are kept fixed during the calibration of other model components – represented by gray rounded shapes – against the calibration datasets (red hexagons). (For interpretation of the references to color in this figure legend, the reader is referred to the web version of this article.)

Sections 3.2–3.9, describe how the data are used by the model as input, for parameter estimation and for model validation. An overview about how the local data are used for calibration of TOPKAPI-ETH parameters is provided in Fig. 2.

3.1. The glacio-hydrological model TOPKAPI-ETH

The model used in this study is the process-oriented, distributed model TOPKAPI-ETH. The model has been applied in numerous hydrological studies of high-elevation watersheds in the Andes [73,74], Alps [18–20] and Karakorum [66,75]. In this study, TOPKAPI-ETH is applied with a grid resolution of 100 m and an hourly temporal resolution. In comparison with previous TOPKAPI-ETH applications, the model structure is identical except for the new glacier debris component, which now allows taking into account the effect of a spatially variable debris thickness on melt. The most important model components and parameters are listed in Table 3. Details about the model components are presented in Sections 3.3–3.8.

3.2. Input data

The model requires air temperature, precipitation and cloudiness as input data. Hourly temperature and precipitation are measured in Kyangjing (Fig. 1) at AWS K and extrapolated to every model grid cell (see Section 3.3). The ratio of measured incoming shortwave radiation and modeled potential clear-sky radiation at AWS K is used to calculate cloud transmissivity (*CT*) factors. Potential clear-sky global irradiance is simulated with a non parametric model based on Iqbal [44] accounting for the position of the sun relative to every grid cell at each time step. The vectorial algebra approach proposed by Corripio [17] is used for the interaction between the solar beam and terrain geometry. The hourly CT factors, which are constant in space, multiply the modeled clear-sky incoming shortwave radiation.

The high temporal resolution chosen constrains the possible simulation period, as AWS K providing the hourly input data was installed on 1 May 2012. We use the period between 1 May 2012 and 17 Nov 2012 to initialize the model. The annual water balance and runoff simulations are calculated for the period 18 Nov 2012–17 Nov 2013.

3.2.1. DEM, glacier and debris maps

A 30 m resolution ASTER Global Digital Elevation Model (GDEM) dataset (available on <http://gdem.ersdac.jspacesystems.or.jp>) resampled to 100 m resolution is used in this study. The vertical accuracy is between 10 and 15 m in area with slopes less than 30° [26,60].

For the debris covered glaciers in the valley, accounting for 82% of the total glacier area, the debris and glacier maps are provided by Pellicciotti et al. [68], where glaciers were manually delineated using three Landsat scenes from 2008, 2009 and 2010. For other glaciers, we use information from two available regional glacier maps: (i) a map based on a semi-automated object-based classification method using Landsat TM7 imagery around the period 2003 [3]; and (ii) a map of manually delineated glacier outlines based on Landsat images taken from 1999 to 2003 [61]. The final glacier and debris maps are shown in Fig. 1a. Since the simulation period in this study is only 1.5 years, no changes of glacier or debris area over time are assumed.

3.3. Extrapolation of meteorological input data

Temperature is extrapolated to every grid cell using hourly lapse rates calculated between air temperature measured at AWS K (3862 m asl) and AWS Y (5090 m asl). Seasonal and diurnal variability of temperature lapse rates in the Langtang valley are discussed in detail by Immerzeel et al. [43].

To account for the cooling effect of snow and ice surfaces, when extrapolated air temperatures over these surfaces are above 0 °C, the lapsed air temperatures are corrected with the parameter T_{mod}. T_{mod} is constant and calculated from the mean difference between air temperature extrapolated at AWS Y and measured at AWS Y-G (Table 3). Local air temperature variations over debris are also accounted for with a constant parameter ($T_{moddebris}$), as debris has been shown to warm up to very high values during the day

Table 3
Summary of all TOPKAPI-ETH parameters that are included in the calibration scheme (Fig. 2).

Name	Unit	Description	Value(s)	Reference or calibration data	Comments
Distribution of meteorological input					
PGv	% km^{-1}	Vertical precipitation gradient	Seasonal	AWS K, Pluvio, Tipping buckets	Values as in [43]
PGh	% km^{-1}	Horizontal precipitation gradient	Seasonal	AWS K, Pluvio, Tipping buckets	Values as in [43]
LR	°C m^{-1}	Temperature lapse rate	Hourly	AWS K, AWS Y	Measured hourly lapse rates
T_{mod}	°C	Temperature decrease over snow and bare- ice	0.71	AWS Y, AWS Y-G	Mean difference between lapsed temperatures from AWS Y and measured at AWS Y-G; standard deviation 0.46 °C
$T_{moddebris}$	°C	Temperature increase over glacier debris	0.75	AWS K, Lirung T-Loggers	Mean temperature difference between lapsed temperatures and interpolated temperatures between Lirung T-Loggers, debris covered Lirung Glacier tongue, 1 May–30 Sep 2013. Standard deviation over 117 grid cells: 0.07°C
Avalanching					
SGR_a, SGR_C	m, –	Snow holding depth dependent on the slope angle; exponential regression function	250, 0.17245	Landsat snow cover	Calibration against avalanched snow cover on the Lirung debris covered glacier tongue, 9 and 25 Oct 2013: mean difference in snow cover 0.01 km^2 or 6.25%
Snow-& ice melt					
α_1	–	Albedo of fresh snow	0.83	AWS Y	Mean measured fresh snow albedo at AWS Y of 12 snowfall events in 2013; standard deviation 0.04
α_2	–	Decay of snow albedo	0.34	AWS Y, Yala stakes	(1) Calibration simulated against measured albedo at AWS Y, 20 April–24 June 2013, RMSE 0.16. (2) calibration against Yala MB (Fig. 4)
α_{reset}	mm d^{-1}	Threshold precipitation rate to reset snow albedo	1	AWS Y	Minimum precipitation rate of 12 observed snowfall events in 2013 at AWS Y
$\alpha_{glacier}$	–	Albedo of bare-ice (glacier surface)	0.25	AWS Y-G	Mean measured value; standard deviation 0.03
SRF		ETI melt model (Eq. (1))	0.00625	Yala MB, Lirung Q	Calibration results in Fig. 4
TF		ETI melt model (Eq. (1))	0.18	Yala MB, Lirung Q	Calibration results in Fig. 4
T_T, P_T	°C	Threshold temperature for melt onset and for for precipitation state transition	1	Literature	With daily time steps often around 0°C [11,39,48], but higher values with hourly time steps (snow depth observations by sonic ranging sensor and measured temperatures at Pluvio)
Subdebris ice melt					
TF_{d1}, TF_{d2}		Debris-ETI melt model (Eq. (2) and (4))	0.03, 0.8	AWS L-G, Energy balance melt model (EB model)	Calibration results in Figs. 3 and 4
SRF_{d1}, SRF_{d2}		Debris-ETI melt model (Eq. (2) and (5))	0.005, 7	AWS L-G, EB model	Calibration results in Figs. 3 and 4
lag_1, lag_2	m^{-1}, –	Debris-ETI melt model (Eq. (2) and (3))	16, 2	AWS L-G, EB model	Calibration results in Figs. 3 and 4
α_{debris}	–	Debris albedo	0.15	AWS L-G	Median of measured debris albedo at AWS L-G, 10 May to 22 Oct 2013, standard deviation 0.03
d	*m*	Debris thickness	0.1–2.5	UAV, EB model, field data Lirung	See Fig. 4
Glacial meltwater routing					
K_{ice}	*h*	Storage constant for ice melt	72	Lirung Q	Calibration results in Fig. 4
K_{snow}	*h*	Storage constant for snowmelt on glaciers	240	Lirung Q	Calibration results in Fig. 4
Evapotranspiration					
CropF	–	Crop factors of evapotranspiration	0.05–1.30	Literature	Calibration against measured actual evapotranspiration (ETA) in Kyangjing by Sakai et al. [81], 15 July–29 August 1996. Simulated ETA during the same period in 2013: 95.3% of measured ETA in 1996
ET_{debris}	%	Evaporation from glacier debris, per mm monsoon precipitation	25	Literature	Value adopted from Sakai et al. [81]

[13]. The correction is based on observations at temperature loggers installed on Lirung Glacier during the monsoon period in 2012 and 2013 (Fig. 1b, Table 3).

Seasonal horizontal and vertical precipitation gradients are taken from [43]. The study found vertical precipitation gradients in the Langtang valley with between 31%–53% precipitation increase per kilometer vertical distance, depending on the season of the year. The horizontal valley gradient was derived from precipitation data recorded at tipping buckets (Fig. 1a) installed in the upper Langtang valley but was found to be relatively weak (mostly less than ±0.6% per kilometer). Previous modeling studies [41,42,48,49] have used a stronger horizontal valley gradient of −3% km^{-1}, based on observations by Shiraiwa et al. [84]. No new data are available in the eastern half of the catchment (Fig. 1a), and the observations by Shiraiwa et al. [84] are only based on snow pack data from five locations in the winter 1989/1990. Thus, we test the effect on simulated streamflow and snow cover of different assumptions of horizontal precipitation gradients upstream of the easternmost tipping bucket (Numthang), after calibration of all other model parameters. The horizontal precipitation gradients are tested independently for pre-monsoon/monsoon (March–September) and for post-monsoon/winter (October–February).

3.4. Avalanching

Gravitational snow transport is modeled using the approach by Bernhardt and Schulz [7], where a maximum snow holding depth is defined as an exponential function of slope. Snow exceeding

the threshold depth is moved to the next model grid cell downwards. The two parameters of the exponential regression function (SGR_a, SGR_C) need to be calibrated. Since for safety reasons it is impossible to measure the maximum snow holding depth in the field, modeled avalanche patterns are calibrated against Landsat ETM+ snow cover (SC) data at the upper end of the debris covered Lirung Glacier tongue. The area above Lirung tongue has a mean slope of more than 100% and ranges from 4500 to 7200 m asl. It is known from field observations that avalanches are very common at this location after major snowfall events and avalanche cones are large enough to be identified by Landsat 30 m resolution imagery. Two Landsat SC images from October 2013 are chosen for comparison (October 9th and 25th). Twelve more images from 2013 would be available, but are not suitable for comparison due to clouds or extensive snow cover. The scene from 9 October 2013 shows only 1.4% snow cover in the catchment for the elevation range 4365–4520 m asl (which comprises the upper end of Lirung tongue), while at the same elevation on Lirung Glacier 71.4% of the area was snow covered. For calibration of the avalanching model component, TOPKAPI-ETH is run for more than 150 possible parameter combinations of SGR_a and SGR_C. Other model parameters are independently defined (Fig. 2) and maintained constant. The optimal parameter combination is determined by choosing the model run which shows the lowest mean difference in total snow cover over the debris covered tongue.

To constrain the possibility that the simultaneous calibration of snow and bare-ice melt parameters (Section 3.5) affects the calibration of gravitational snow transport parameters, we perform several calibration iterations. The iteration loop ends when optimal parameters SGR_a and SGR_C do not vary anymore from one iteration to the next.

3.5. Snow- and bare-ice melt

Snow- and bare-ice (debris-free) melt is computed using an Enhanced Temperature-Index (ETI) approach [64,65]:

$$M_i = \begin{cases} TF \cdot T_i + SRF \cdot I_i \cdot (1-\alpha_i) & T_i \geqslant T_T \\ 0 & T_i < T_T \end{cases} \quad (1)$$

Melt (M, mm w.e. h^{-1}) in each grid cell i is a function of an air temperature (T, °C) dependent term including an empirical temperature factor TF (mm w.e. h^{-1} °C^{-1}) and a shortwave radiation dependent term that uses the distributed incoming shortwave radiation (I, Wm^{-2}), an empirical parameter SRF (m^2mm w.e. W^{-2} h^{-1}) and snow or ice albedo (α). T_T is the threshold air temperature for melt onset.

Bare-ice albedo is constant in space and is calculated as the mean ratio of incoming and reflected shortwave radiation measured at AWS Y-G during June 2012. The decrease of fresh snow albedo (α_1) is modeled as a logarithmic decay in function of cumulated daily maximum positive air temperatures, controlled by an empirical parameter α_2 [12]. Each time precipitation exceeds a snowfall threshold rate α_{reset}, snow albedo is reset to α_1. The parameters α_1, α_2 and α_{reset} are estimated using data measured at AWS Y. Details are provided in Table 3.

The parameters TF and SRF are calibrated simultaneously against the observed mass balances at eight ablation stakes on Yala Glacier and against measured runoff at the outlet of the Lirung Glacier subcatchment (Fig. 2). The advantage of this approach is that the uncertainty in parameter identification can be reduced by evaluating the model against a number of responses representing different aspects of the hydrological functioning of the catchment (e.g. [2]). The effect of potential measurement errors on optimal parameters can also be mitigated [5].

Lirung runoff data are discussed in Section 3.7. The mass balance obtained from stake readings between 10 November 2011 and 3 November 2012 and the location of the stakes on Yala Glacier are described in [4]. The present study uses stake readings from 3 November 2012, 8 May 2013 and 18 November 2013. The mass balances calculated between 3 November 2012 and 8 May 2013 are not used for calibration, to prevent possible error compensation due to inaccuracies in simulated winter snow accumulation.

The parameter α_2 is also included in the calibration against Yala mass balance observations (5190–5501 m asl), to obtain a second estimate of snow albedo evolution. Albedo parameters are kept constant when calibrating TF and SRF against Lirung runoff. Therefore, an optimal α_2 is determined for each pair TF-SRF on the basis of the Yala mass balance data, and this α_2 is then used for each pair TF-SRF during calibration against Lirung streamflow.

3.6. Sub-debris ice melt

The presence of supraglacial debris strongly affects ablation (e.g. [13,62,95]). For this study, TOPKAPI-ETH was modified to account for the debris thickness feedback on melt. The sub-debris ice ablation model implemented is based on work by Mabillard [54] and has been tested on Miage and Arolla glacier in the Alps [15]. Ice melt below debris is calculated using a modified version of the ETI melt model that can take into account the melt reducing effect of varying debris thickness and hereafter is called debris-ETI (dETI) model:

$$M_i(t) = \begin{cases} TF_d \cdot T_i(t-lag) + SRF_d \cdot I_i(t-lag) \cdot (1-\alpha_i) & T_i \geqslant T_T \\ 0 & T_i < T_T \end{cases} \quad (2)$$

where $M_i(t)$ is simulated melt (mm w.e. h^{-1}) for each grid cell i and time step t, T is air temperature (°C), I is incoming shortwave radiation ($W\,m^{-2}$), α is debris albedo and T_T is the threshold air temperature for melt onset. In contrast to the original ETI equation (Eq. (1)), a parameter lag has been introduced. This parameter has a unit h and varies in function of debris thickness, to take into account that the effect of air temperature and shortwave radiation on melt is temporally delayed by the debris:

$$lag = lag_1 \cdot d - lag_2 \quad (3)$$

where d is debris thickness (units of m) and lag_1 and lag_2 are two empirical parameters. Both SRF_d and TF_d (Eq. (2)) also vary with debris thickness:

$$TF_d = TF_{d1} \cdot d^{-TF_{d2}} \quad (4)$$

$$SRF_d = SRF_{d1} \cdot e^{-SRF_{d2} \cdot d} \quad (5)$$

TF_{d1}, TF_{d2}, SRF_{d1} and SRF_{d2} are empirical parameters which need to be calibrated. The physics of the energy exchange between surface and atmosphere and within the debris layer is best represented by physically-based models. Energy balance (EB) models have very good performance when high quality input data are available (e.g. [65,76]), but their use is more questionable at the distributed scale or with extrapolated data [28]. We therefore assume that a dEB model provides the best estimates of ablation at the location of AWS Lirung Glacier (AWS L-G). The dETI model is compared to the debris-EB (dEB) model of Reid and Brock [76] at AWS L-G to ensure appropriate parameter selection. To test the validity of the dEB model, modeled surface temperatures were validated against measured data [92]. This study uses the dEB results for a debris thickness range of 0.1–2.5 m and for the period 19 May 2013–21 Oct 2013 (Fig. 3). The parameters of the dETI model are calibrated against the outputs of the dEB model by minimizing the mean of the root mean square error of hourly melt rates for the tested range of debris thickness.

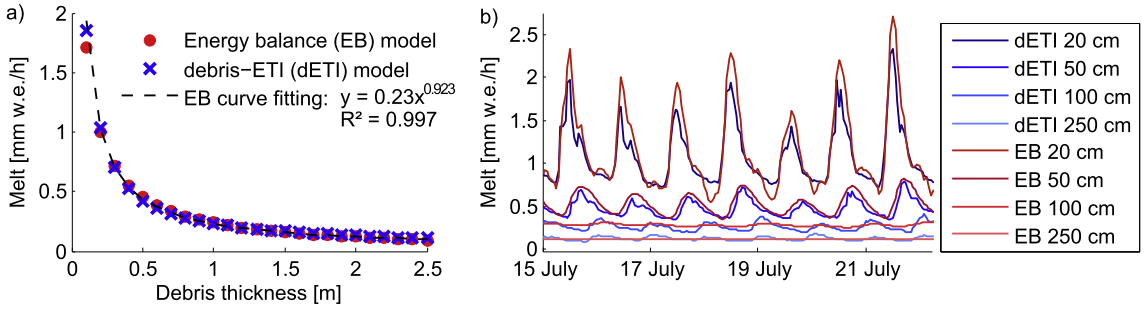

Fig. 3. (a) Energy balance (EB) and debris-enhanced temperature index (dETI) melt model outputs for given debris thicknesses (simulations for the period 19 May 2013–21 Oct 2013). The dashed line represents the Østrem curve that has been fitted to the results of the EB model. (b) Close-up view of model results corresponding to debris thicknesses of 20, 50, 100 and 150 cm for the period 15–22 July 2013.

More than 350'000 possible parameter combinations of lag_1, lag_2, TF_{d1}, TF_{d2}, SRF_{d1} and SRF_{d2} were tested.

3.6.1. Debris thickness estimation

The surface properties of a debris covered glacier are highly heterogeneous, with a rugged topography, ice cliffs and supraglacial ponds [6,68]. Ground-based observations of debris thickness can only provide a rough estimate of the debris thickness distribution, and were conducted only on Lirung Glacier (the transects where debris thickness was mapped are shown in Fig. 1b). The debris was mostly too thick to be sampled by manual methods (in 92.8% of all cases debris was thicker than 50 cm). Debris thickness can be estimated by methods that are based on remote sensing such as the ones described by Mihalcea et al. [55], Zhang et al. [95], and Foster et al. [21] or by Fujita and Sakai [23]. Empirical methods such as Mihalcea et al. [55] are site specific and require large amount of in situ data for calibration. The more physically based method by Foster et al. [21] failed to reconstruct the thick debris of Lirung Glacier, likely because of the assumption of a linear temperature gradient within the debris and lack of knowledge of surface temperature distribution [69]. In this study, we therefore propose a new approach that makes use of several available datasets to map debris thickness.

First, two high resolution DEMs obtained from UAV flights at the beginning (19 May) and at the end (21 Oct) of the ablation season 2013 are used to quantify the mass loss at Lirung Glacier glacier between the two dates. The glacier surface height changes are aggregated to the TOPKAPI-ETH 100 m grid and converted into meter water equivalents (m w.e.) of melt assuming a density of ice of 900 kg m^{-3}. The Østrem curve is derived using the dEB model at the location of AWS L-G as described in Section 3.6. This curve (equation indicated in Fig. 3a) is used to assign a debris thickness to each TOPKAPI-ETH glacier grid cell in the UAV survey from the cell ablation rate, assuming that the Østrem curve is the same over the entire tongue.

Vertical emergence of the glacier would cause an error in the quantification of ice loss and therefore in the debris thickness estimates. Overall this error is likely to be limited as the flow velocity of the Lirung Glacier is very small [40]. However, there is a small region near AWS L-G (Fig. 1b) where emergence occurs [40]. From field observations we know that this area is characterized by thick debris cover. In order to prevent unrealistic debris thickness values due to very small elevation changes or increasing surface height, maximum debris thickness is limited to 2.5 m.

The inverse Østrem approach is used to calculate debris thickness on the lower half of the Lirung Glacier tongue, in the area covered by the UAV survey (Fig. 1b). Then, the thickness of all debris covered glacier areas are sampled from the debris thickness estimates from Lirung Glacier, and satellite imagery is used to distinguish between the most important debris surface characteristics for the random sampling. The presence of lakes and ice cliffs affect the reconstructed debris thickness estimates, and they are taken into account in an indirect way. A supraglacial lake map from May 2012 is thus used to identify the concentration of supraglacial ponds. A map of supraglacial cliffs is not available, thus we assume that the fraction of cliffs correlates with the presence of lakes [95]. If a 50 m elevation band of a debris covered glacier includes supraglacial ponds, the debris thickness of those grid cells is sampled randomly from 50 m elevation bands within the UAV survey area that do include ponds. The same is done for 50 m elevation bands that do not include ponds, and separately for the lowest 50 m elevation band of each debris covered glacier, in order to account for the effect of frontal ablation on reconstructed debris thickness. The spatial density of supraglacial lakes and cliffs is thus used as a proxy for spatial variations in the equivalent debris thickness when sampling the debris thickness estimates from Lirung Glacier. The supraglacial lake map is described in Pellicciotti et al. [68] and is constructed from Landsat ETM+ multispectral data. The locations of the ponds are indicated in Fig. 1a.

Few previous studies have shown a mild dependency of debris thickness on elevation [21,47,95], but these relationships were all obtained along one longitudinal profile neglecting the transverse variability, which our field observations showed was large. At Lirung Glacier, thick debris accumulated through rockfall and avalanches appears right below the glacier cirque. On the basis of our observations from the field a gradual increase of debris thickness along the entire glacier is not evident for such glaciers. Due the lack of an established functional dependence of thickness on elevation or other topographical variables we thus apply the random sampling approach described above. However, 12.9% of the total debris covered area at the upper end of the tongues is excluded from the random sampling, and only a shallow debris thickness of 0.1 m is assumed here (Fig. 1a) in accordance with the results of Zhang et al. [95], who found that debris thickness varied between 0 and 20 cm in the uppermost section of debris covered area. We assign such shallow debris thickness to glacier area where a discrepancy exists between the manually and a automatically [63] delineated debris cover map, assuming that only the manual method correctly classifies the shallow debris cover of such areas.

3.7. Glacier meltwater routing

Meltwater from the glacier is routed to the glacier outlet (i.e. the lowest grid cell of the glacier) using the linear reservoir approach, which has been commonly used for the transformation of surface meltwater into glacier discharge (e.g. [32,45,73]). We distinguish two reservoirs for snow and ice, respectively. The two storage coefficients (K_{snow} and K_{ice}) are calibrated together with the melt parameters *TF* and *SRF* against hourly runoff measured between 1 May 2013 and 17 Nov 2013 at the outlet of the Lirung

subcatchment (prior to this period the stream was frozen). More than 1500 possible combinations of the parameters *TF*, *SRF*, K_{snow} and K_{ice} are tested. The Nash–Sutcliffe (N&S) efficiency criterion [58] is used for model evaluation. As a second criterion, we reject all parameter combinations that result in a mean daily runoff amplitude higher or lower than ±50% of the measured mean daily amplitude.

As 71.3% of the Lirung subcatchment area is glacierized, it can be assumed that the independent calibration of evapotranspiration parameters (Section 3.8) does not interfere with the calibration of storage coefficients and melt parameters.

3.8. Evapotranspiration and drainage

Water routing outside the glacier areas is based on the kinematic wave concept, whereby soil drainage and channel- and overland flow are represented by nonlinear reservoir differential equations [51,52]. The soil-, surface- and channel routing is based on properties that in theory are physically measurable. However, soil and surface roughness parameters aggregate spatially and temporally heterogeneous properties of the real system. The aggregate nature of parameters makes it difficult to specify them directly and unambiguously from point observations made in the field. Considering the large number of properties that need to be specified (eight parameters per soil type and layer), a systematic identification of soil parameters on the basis of in situ data or through calibration is thus difficult. Soil parameters for this study are therefore exclusively estimated based on literature [19,75,82]. We define nine different soil classes (assigned as a function of three slope categories and thee elevation categories) and two soil layers. The suitability of the soil configuration and the standard parameters to represent seasonal soil water storage is discussed in Section 5.2.

Potential evapotranspiration from non-glacierized cells is calculated using the Priestly–Taylor equation [71], in which net radiation is assumed to be a function of incoming shortwave radiation, albedo, and air temperature through an empirical equation. Crop factors (*CropF*) determine the potential crop evapotranspiration. Actual evapotranspiration (ETA) depends on the available soil moisture content within the superficial soil layer, which is calculated by the model. Since no recent field observations of ETA are available, the modeled ETA at Kyangjing (Fig. 1a) is compared to the magnitude of lysimetric estimates by Sakai et al. [81] during the monsoon period (Table 3). The same publication also provides an estimate about evaporation from glacier debris. The estimate of 25% evaporation of liquid precipitation on debris covered glacier area during the monsoon period is considered by subtracting that amount from precipitation over debris.

3.9. Model validation

At the outlet of the upper Langtang catchment (Fig. 1a), hourly discharge is estimated from stage heights recorded by a radar water level sensor (Ott RLS) at 15-min intervals. In contrast to most glacio-hydrological studies, catchment runoff is not used for parameter calibration, and can thus be used for model validation.

A second dataset that has not been used for calibration and that is used for model validation is observed fractional snow cover (fSC) data from MODIS and Landsat imagery. MYD10A1 and MOD10A1 data from the MODIS Aqua and Terra platforms with 500 m resolution are downloaded from <www.nsidc.org>. Images with more than 10% cloud cover over the study catchment are discarded due to the risk of cloud/snow confusion [30,31,91]. TOPKAPI-ETH fSC is then calculated for each corresponding 500 × 500 m MODIS grid area. The root mean square error of daily snow cover is calculated using the minimum difference between simulated and observed fSC at each MODIS grid cell, comparing simulated fSC at 9 am and at 17 pm. Landsat fSC is also calculated for the MODIS 500 × 500 m areas, so that TOPKAPI-ETH fSC can be validated also against Landsat (although only available for a few dates), and Landsat can be compared against MODIS. The advantage of using the MODIS fSC product rather than the binary product is that small scale variation in SC (typical for high-elevation areas, e.g. [74]) modeled by TOPKAPI-ETH and observed by Landsat do not have to be averaged out for comparison against MODIS.

3.10. Sensitivity analysis

In order to test the effect of parametric uncertainty on simulated streamflow volumes, we perform a regional sensitivity analysis [35,85]. TOPKAPI-ETH is run in a Monte-Carlo way with 1000 parameter sets where the parameters of the model are varied randomly within ±10% of their calibrated value (or ±0.1 °C for parameters with temperature units). The Monte-Carlo simulations are used to evaluate the effect of relative changes in single parameters on the model outputs. Following the approach of Ragettli et al. [75], the 1000 parameter sets are partitioned in two groups: parameter sets that lead to more than average and to less than average simulated streamflow volumes, over a certain time period. The maximum vertical distance between cumulative distribution functions (CDFs) of single model parameters within the two groups is used to assess if a parameter significantly contributes to the resulting uncertainty in simulated streamflow, a property which hereafter is called 'information content' (IC). Soil-, routing- and evapotranspiration parameters are excluded from the information content analysis since the focus of this study is on the cryospheric processes that affect the annual water balance. Precipitation gradients and temperature lapse rates are also excluded since it has already been shown previously that the model is very sensitive to those parameters in the upper Langtang catchment [43].

To identify the characteristics of the catchment (such as elevation, slope or debris cover) that increase the model sensitivity, we calculate the information content distribution in space [75]. Areas of high information content indicate the locations where information about the hydrological system can most efficiently constrain runoff uncertainty. For this spatial IC analysis we look at the difference between cumulative distribution functions (associated with the two groups of parameter sets) of the simulated mass balance in each glacier grid cell (hereafter called 'cell information content'). We calculate also the mean cell information content for each glacier and put the result in relation to glacier characteristics (such as mean elevation, slope or debris cover; Table 1).

4. Results

4.1. Parameter calibration

The results of the parameter calibration are shown in Table 3. For constant parameters that are estimated directly on the basis of measured data, standard deviation in measured parameter values are provided (T_{mod}, $T_{moddebris}$, α_1, $\alpha_{glacier}$, α_{debris}).

Over the monitored period, the dETI model reproduces energy-balance modeled melt with a mean difference of 0.019 mm w.e. h^{-1} (Fig. 3a). The largest differences occur for debris thicknesses of 0.1 m, where the dETI model overestimates total melt by 550 mm w.e. over the ablation period (0.15 mm w.e. h^{-1}). However, this error is negligible considering that reconstructed mean debris thicknesses over the Lirung tongue are never less than 0.2 m (see Section 4.2). Diurnal melt rate variability and amplitude estimated from the EB model overall are well-simulated by the dETI model (Fig. 3b). Diurnal melt rate variability in debris thicker

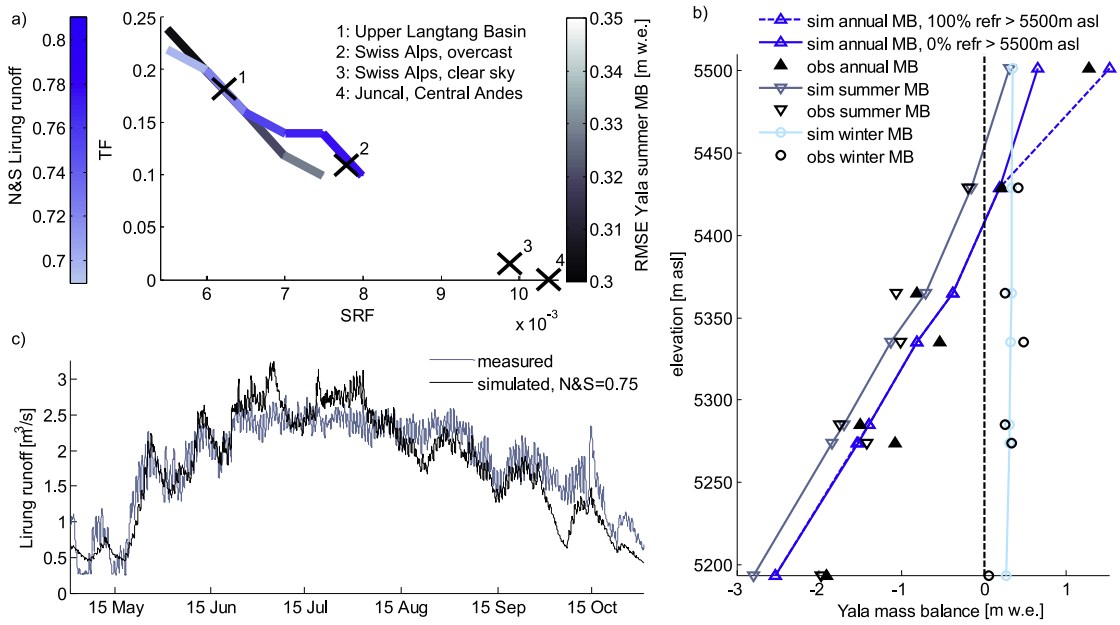

Fig. 4. (a) Optimal parameter combinations of the parameters *SRF* and *TF* for various places on Earth [14], reflecting the dependence of the parameters on local climatic conditions. The colored lines indicate the highest achieved model efficiency (Nash–Sutcliffe, *N&S*, of simulated Lirung runoff, and root mean square error, *RMSE*, with respect to Yala mass balance observations) and parameter *TF* that corresponds to each tested value of *SRF*. The parameter combination where the two lines cross is assumed to represent the optimal solution for the Upper Langtang Basin. (b) Simulated (sim) and observed (obs) summer (8 May 2013–18 Nov 2013), winter (3 Nov 2012–8 May 2013) and annual Yala mass balance (MB). The blue dotted line connects the simulated annual MB that was calculated assuming 100% refreezing of meltwater above 5500 m asl. (c) Measured and simulated runoff at Lirung streamgauge. Model results shown in (b) and (c) are simulated using a parameter combination $SRF = 0.00625$ and $TF = 0.18$.

than 1 m is overestimated by the dETI model, but the magnitude of daily melt is similar.

The melt factors SRF and TF are calibrated simultaneously against Yala summer mass balance (MB) stake observations and Lirung runoff (Fig. 4). The calibration against Lirung runoff results in an optimal *SRF* which is higher, and an optimal *TF* which is lower than the corresponding parameters calibrated against Yala MB. Several parameter combinations result in an acceptable model performance (N&S higher than 0.7, RMSE Yala MB lower than 0.35 m w.e.). To identify the best combination with respect to both datasets, we look at the highest model efficiency and values of TF that correspond to each tested value of SRF (Fig. 4a). For an *SRF* value of 0.00625 calibration against both datasets yields an optimal value of *TF* of 0.18. It is therefore assumed that this parameter combination represents the optimum of all possible parameter combinations, given the differences in meteorological conditions, possible modeling and measurement errors that may have led to the differences in model results.

The modeled Yala Glacier MB and Lirung discharge for *SRF* equal to 0.00625 and *TF* equal to 0.18 are presented in Fig. 4b and c. Note that the observed Yala winter MB was not used for calibration (Fig. 4b). As only annual MB is observed at 5501 m asl we do not use this point for calibration. The modeled annual MB at this location exhibits the largest departure from observations (underestimation by 0.6 m w.e.). It is possible that at this elevation, which was above the equilibrium line altitude (ELA), meltwater refreezes in the snow layer [56]. Model results are therefore also shown for the assumption that 100% of melted snow refreezes at 5501 m asl, which yields a better result comparing to the MB observations. The largest error in simulated summer MB appears at the elevation of the lowest ablation stake, at 5194 m asl (simulated MB more negative by 0.7 m w.e.). However, the MB measurements are affected also by small scale topography and wind-effects that cannot be reproduced by the model, as well as by measurement errors.

The comparison of measured with simulated runoff at the outlet of the Lirung subcatchment (Fig. 4c) reveals that the model overestimates the inter-seasonal variability of runoff, especially for the period after 1 July 2013. Increasing the storage coefficients (optimal values presented in Table 3) can smooth out the inter-seasonal variability but would lead to further underestimation of the daily runoff amplitude.

4.2. Reconstructed debris thickness and melt below debris

Mean reconstructed debris thicknesses for the Lirung tongue are shown in Fig. 5 together with modeled and observed surface height change as a function of elevation. Only one 50 m elevation band contains a supraglacial pond ('Lake 1') that can be identified from Landsat ETM+ data. Debris thickness of debris covered glacier area including lakes but not mapped by the UAV flights is thus sampled from there (Section 3.6.1). This Section (4070–4120 m asl) is characterized by variable but relatively low debris thickness (mostly less than 1 m). Another large supraglacial pond ('Lake 2') is just above the UAV mapped area, but smaller ponds and many cliffs follow in glacier flow direction (4170–4220 m asl). This section of the glacier is characterized by reconstructed debris thicknesses between 1 and 2 m. The lowest debris thickness values (0.2–0.9 m) are calculated for the area near the glacier snout. The reconstructed debris thickness has to be understood as a proxy for all surface features of debris covered glacier area that contribute to melt (Section 3.6.1). Our observations show that debris covered glacier area with a more rugged surface – and therefore more supraglacial ponds – experiences more pronounced glacier surface changes over the ablation season (Fig. 5). This is respected by the model even though no information about supraglacial cliffs and their contribution to glacier melt is available.

Fig. 5 also shows comparison of modeled surface change to observed surface changes. Overall the agreement is very high, with a mean error in simulated surface change of 0.16 m (equivalent to a

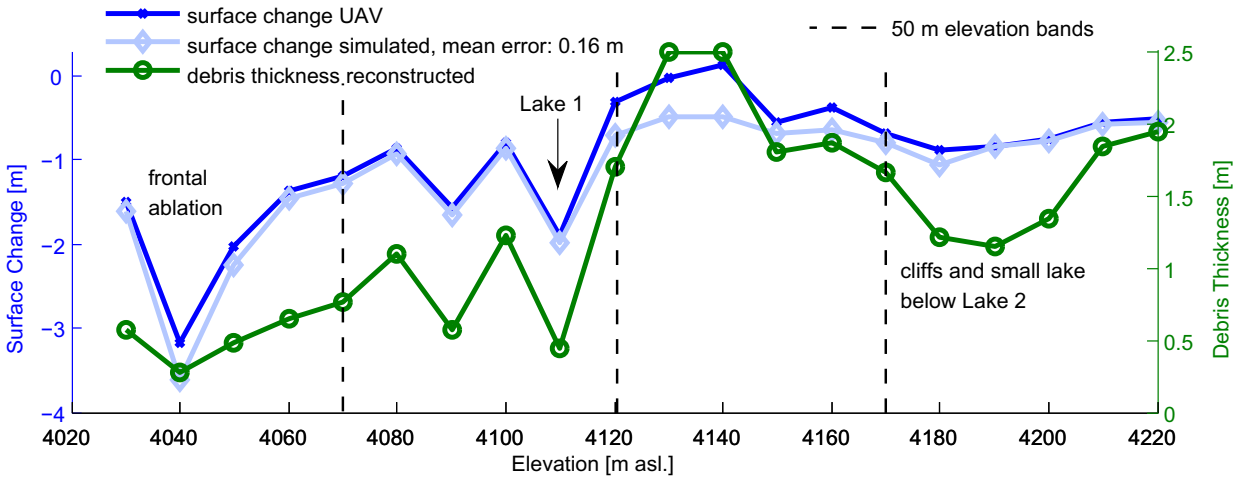

Fig. 5. Surface height changes documented by an Unmanned Aerial Survey System (UAV) between 19 May and 21 October 2013, simulated surface changes corresponding to the same period assuming an ice density of 900 kg m^{-3}, and reconstructed debris thickness. The figure shows mean values for each 10 m elevation band of Lirung Glacier. 50 m elevation bands are used to assign different categories of debris covered area (frontal ablation, supraglacial lake area or not supraglacial lake area) to debris outside the UAV range (Fig. 1b) for the random sampling of reconstructed debris thickness values.

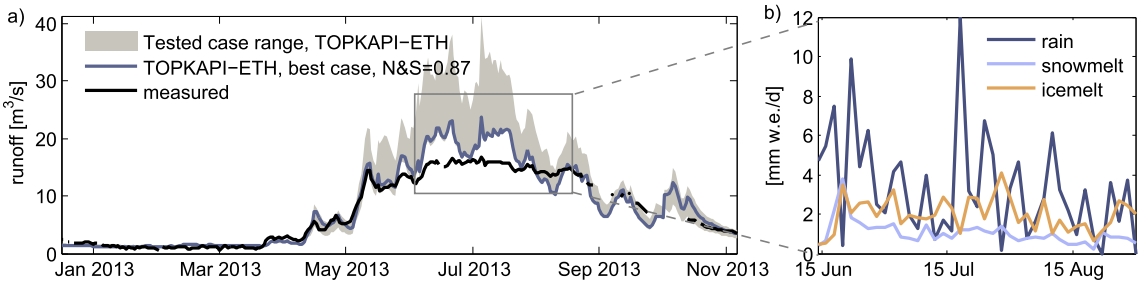

Fig. 6. (a) Simulated and measured daily runoff at Langtang Khola streamgauge. The tested case range corresponds to the model outputs simulated with the tested model setups indicated in Table 4. The 'best case' corresponds to case 8 in Table 4. (b) Running 72 h mean values of water balance components corresponding to case 8 model outputs.

difference of less than 1 mm w.e. ice melt per day). More significant differences to observed surface change appear for very shallow debris thickness (4040 m asl in Fig. 5, 0.5 m difference) and for very thick debris (4120–4140 m asl in Fig. 5, 0.4–0.6 m difference). Note however that the overestimation of surface change at 4120–4140 m asl is partly due to vertical emergence of the glacier at this location [43], so the comparison should be treated with care here. The good results confirm the applicability of the dETI melt model on the distributed scale and suggest a realistic reproduction of air temperature and incoming shortwave radiation during the ablation period in 2013.

4.3. Model validation against remotely sensed snow cover and catchment runoff

The previous two sections showed that the available in situ data could be successfully used to constrain model parameters. However, uncertainty prevails about hydro-meteorological processes in parts of the catchment where no data are available. Model validation against catchment runoff and catchment snow cover thus reveals if the locally collected in situ data is representative also of the rest of the catchment. Moreover, validation against both catchment runoff and snow cover allows testing a range of assumptions about two processes about which no in situ data are available yet: precipitation in the east of the catchment (east of Numthang, see Section 3.3) and melting conditions above 5500 m asl (see Section 4.1). Figs. 6a and 7 present ranges of catchment runoff and snow cover simulated by multiple model runs using the fixed parameters discussed above, but with a horizontal precipitation gradient east of Numthang ($PGh2_{winter}$ and PGh_{summer}) varying between 0 and −10% km^{-1} and a coefficient of refreezing (CFR, % of total melt above 5500 m asl) varying between 0 and 100% (Table 4). The uncertainty in simulated runoff due to the tested assumptions is very large during the monsoon period (around 10 m^3 s^{-1} uncertainty from mid-June to end of July, equivalent to 33% of total runoff, Fig. 6a). The uncertainty in simulated snow cover is mostly around 20% of the catchment area, but more constant in time (Fig. 7).

Goodness-of-fit measures are provided in Table 4. The *N&S* value of the tested assumption varies between −0.5 (case 1: PGh2 zero, CFR 0%) and 0.89 (case 10: PGh2 −10% km^{-1} in summer and winter, CFR 100%). The mean root mean square error (RMSE) in simulated fractional snow cover in comparison to MODIS varies between 41.1% (case 9: $PGh2_{winter}$ and PGh_{summer} −10% km^{-1}, CFR 0%) and 23.6% (case 8: $PGh2_{winter}$ zero and PGh_{summer} −10% km^{-1}, CFR 100%). Note that during the monsoon period, MODIS fSC images are very much affected by clouds and are therefore not used for comparison. Comparison against Landsat SC is also possible, although only few images are available over the year. Here, the tested cases 1–8 perform about equally well (Table 4). Regarding the *N&S* values, cases 6, 8 and 10 perform very well (*N&S* $\geqslant$0.87, Table 4). Considering all criteria together, case 8 can be considered as best performing. Simulated catchment runoff and snow cover using the assumptions associated to case 8 are therefore presented in Figs. 6 and 7 as the best run. Parameter values shown in Table 3 and assumptions about precipitation distribution and melt above

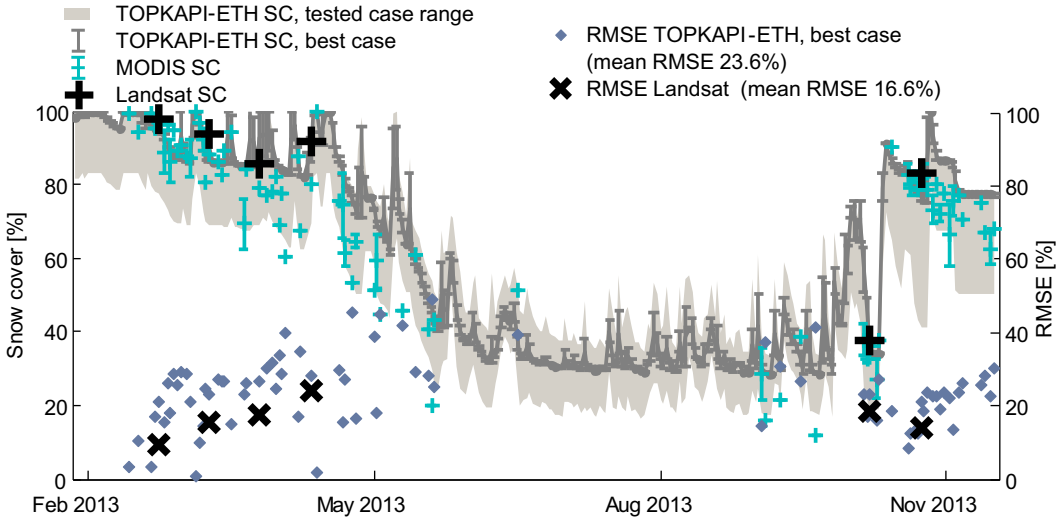

Fig. 7. Remotely sensed MODIS and Landsat snow cover (SC) and snow cover simulated by the model (TOPKAPI-ETH). The tested case range corresponds to the model outputs simulated with the tested model setups indicated in Table 4. The 'best case' corresponds to case 8 in Table 4. The error bars that are shown for MODIS SC correspond to the differences in SC observed by Terra and Aqua satellites. The error bars in 'best case' TOPKAPI-ETH SC correspond to simulated daily fluctuations between 9 am and 17 pm. The TOPKAPI-ETH root mean square error (*RMSE*) is calculated using always the minimum difference between simulated and observed fractional snow cover at each MODIS grid cell. Landsat *RMSE* values are calculated in the same way and should be regarded as a benchmark for model comparison against MODIS.

Table 4
Configuration of model setups that are tested against catchment runoff, MODIS snow cover (SC) and Landsat SC.

Case	PGh2 summer	PGh2 winter	CFR	Runoff N&S	MODIS SC mean RMSE (%)	Landsat SC mean RMSE (%)	Precipitation mm/a	Snowmelt mm/a	Ice melt mm/a	GMB mm/a
1	0	0	0	−0.50	23.9	16.8	1388	581	166	0.23
2	0	0	100	0.14	24.0	16.8	1388	511	164	0.40
3	−3	−3	0	0.07	23.9	17.6	1121	514	192	−0.16
4	−3	−3	100	0.55	24.0	17.6	1121	444	188	0.00
5	−10	−3	0	0.51	24.1	19.7	792	406	272	−0.67
6	−10	−3	100	0.89	24.0	19.6	792	337	244	−0.45
7	−10	0	0	0.47	23.7	17.5	943	441	263	−0.46
8	−10	0	100	0.87	23.6	17.6	943	366	238	−0.23
9	−10	−10	0	0.52	41.1	42.5	658	353	291	−0.86
10	−10	−10	100	0.89	35.7	36.3	658	288	255	−0.62

PGh2 is the horizontal precipitation gradient (% km^{-1}) applied east of Numthang (Fig. 1a), *CFR* is the coeffient of refreezing (%) applied to elevations higher than 5500 m asl. Other parameters are identical to the values indicated in Table 3. N&S is the Nash–Sutcliffe efficiency coefficient and RMSE is the root mean square error. *Precipitation*, *Snowmelt*, *Icemelt* and mean glacier mass balance (*GMB*) represent model outputs.

5500 m asl tested in case 8 are used to model the water balances in the following Section 4.4 and for the sensitivity analysis in Section 4.5.

4.4. Simulated water balance

The simulated magnitudes of all components of the water balance are shown in Fig. 8a and Table 5 for the upper Langtang basin and for the Lirung subcatchment. Total ice melt amounts to 26% of all positive water balance components (providing water input to the hydrological system) for the entire basin (43% for Lirung subcatchment). Snowmelt amounts to 40% (38% for Lirung) and rainfall contributes by 33% (19% for Lirung). The steep topography of the Lirung subcatchment results in a high importance of gravitational snow transport for the annual water balance: 16% of the annual water input originates from melt of snow that has been avalanched (43% of total snowmelt; Fig. 8a). On the larger scale it is only 4.5% of total water input or 11% of total snowmelt. Only 8% of total Lirung ice melt originates from sub-debris ablation (Fig. 8a). This value is substantially higher for other debris covered glaciers (Langtang: 49%, Langshisha: 30%, Shalbachum: 69%). Overall, 33% of total ice melt in Langtang originates from sub-debris ablation, which is equivalent to 8.6% of total water input.

Overall, the water input at Lirung subcatchment is much higher than for the entire basin (1923 mm w.e. in Lirung and 906 mm w.e. in Langtang, Fig. 8a). Measured monsoonal streamflow volumes at Lirung hydrological station amount to 15.8% of measured streamflow at Langtang Khola station, although Lirung subcatchment represents only 4.4% of the total catchment area. This is likely due to decreasing precipitation from west to the east, high elevations and strong vertical precipitation gradients and an important fraction of Lirung Glacier area that has a south aspect and is not mantled in debris.

The magnitude of runoff production decreases from west to east (Fig. 8b). Areas in the east of the study catchment receive very little precipitation in form of rain due to lower temperatures at higher elevations and a strong horizontal precipitation gradient during the warm period. The relative importance of ice melt as a water input increases up-valley. In the northeastern section of the upper Langtang basin (that includes Langtang Glacier) ice melt represents

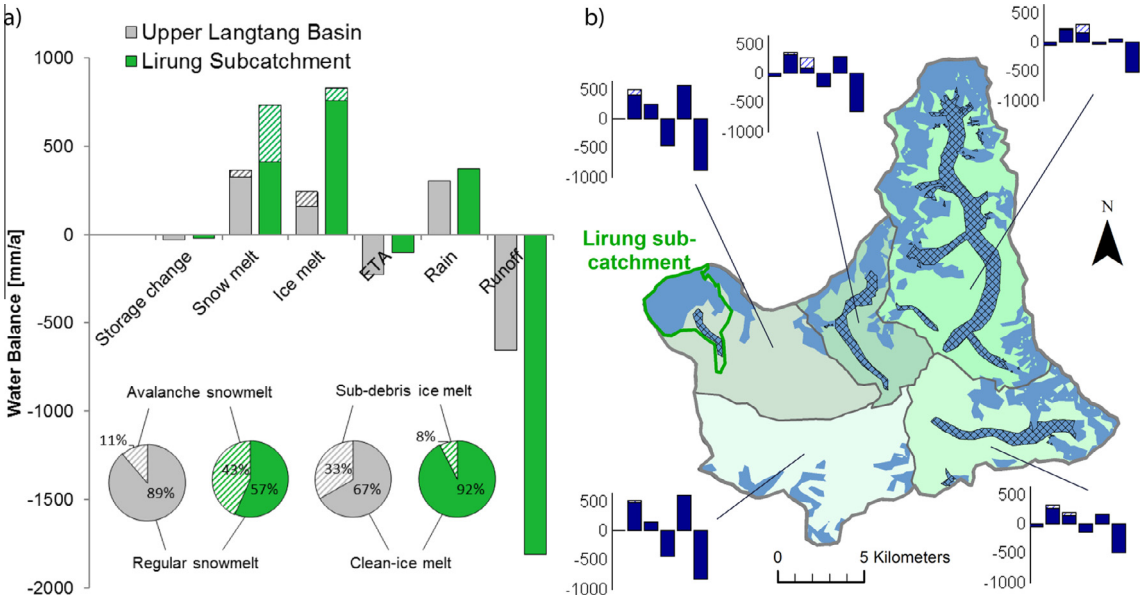

Fig. 8. Simulated water balance for the year 18 Nov 2012–17 Nov 2013: (a) upper Langtang basin and Lirung subcatchment, (b) five sub-sections of the watershed. The components of the water balance are storage changes (soil-, channel-, surface- and englacial reservoir water), snow- and icemelt, evapotranspiration (*ETA*), rain and runoff (always shown in the same order). Hatched patterns show snow- and icemelt from avalanched snow and from debris covered areas, respectively. The sum of positive and negative components of the water balance is always zero.

Table 5
Mean values of the water balance components calculated for (1) the upper Langtang catchment and (2) the Lirung subcatchment.

	Annual		Post-monsoon		Winter		Pre-monsoon		Monsoon	
	(1)	(2)	(1)	(2)	(1)	(2)	(1)	(2)	(1)	(2)
Total inputs										
Rain	305.7	370.7	42.0	37.9	0.0	0.0	30.3	35.1	233.4	297.7
Snow melt										
Regular	324.5	414.9	64.7	48.8	12.5	13.5	181.4	190.4	65.8	162.2
Avalanched	41.2	317.4	0.4	15.9	0.1	2.9	8.4	60.5	32.4	238.1
Ice melt										
Bare-ice	158.6	767.6	3.1	34.8	0.6	7.9	18.7	136.1	136.3	588.8
Sub-debris	79.3	63.5	2.6	6.0	0.2	1.3	12.5	14.9	63.9	41.2
Residuals										
Storage change	−28.6	−21.0	−13.0	32.6	19.2	17.1	−54.2	−74.0	19.6	3.3
Losses										
Evapotranspiration	−228.4	−101.9	−17.1	−6.6	−3.0	−2.4	−61.9	−31.5	−146.3	−61.4
Outflow	−652.4	−1811.0	−82.8	−169.4	−29.6	−40.4	−135.2	−331.4	−405.0	−1270.0

Seasonal values are shown for post-monsoon (1 October–31 November), winter (1 December–28 February), pre-monsoon (1 March–15 June) and monsoon (16 June–30 September) periods of the hydrological year 2012/2013. *Avalanched snow melt* is here defined as snow that would not have melted if it was not transported to lower elevations. *Storage change* represents changes in soil-, channel-, surface- and englacial water reservoirs. Values are expressed in milimeter water equivalents.

Table 6
Results of the regional sensitivity analysis: ranking of parameters regarding their information content for simulated annual and seasonal streamflow volumes.

Rank	Annual	Winter	Pre-monsoon	Monsoon	Post-monsoon	Behavioral
1	SRF	SGR_a	α_1	SRF	α_1	SRF
2	α_1	α_1	SRF	α_1	SRF	α_1
3	T_{mod}	SRF	SGR_a	T_{mod}	T_T	SGR_a
4	SGR_a	T_{mod}	T_{mod}	SGR_a	α_2	T_{mod}
5	T_T	α_2	T_T	T_T	T_{mod}	d
6	TF_{d1}		α_2	TF_{d1}	P_T	TF
7	d			d	SGR_a	TF_{d1}
8	TF			TF		TF_{d2}
9				TF_{d2}		

For the category *Behavioral*, parameters are ranked according to their information content regarding the Nash–Sutcliffe efficiency criteria. Only parameters exceeding the α threshold of the Kolmogorov–Smirnov test are shown. Parameters are described in Table 3.

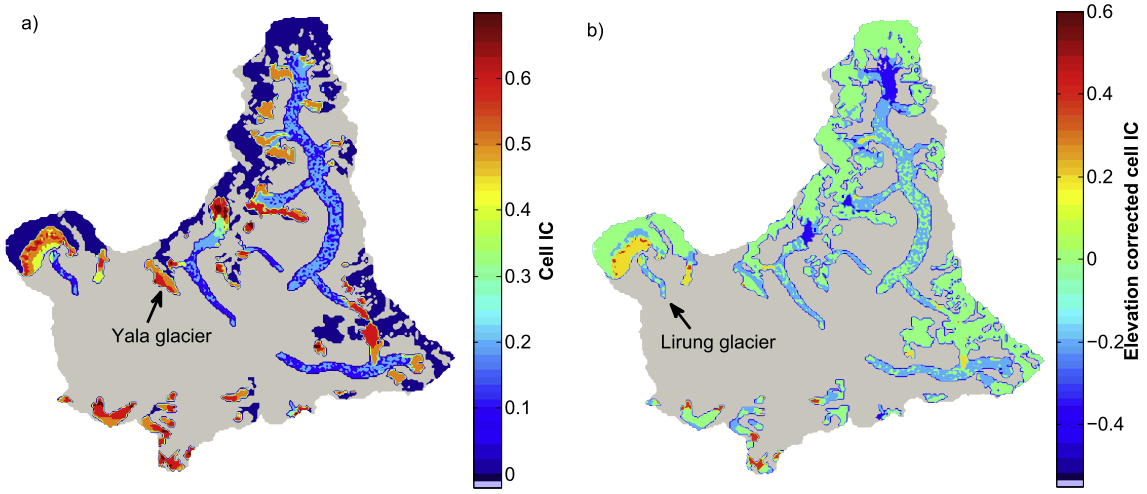

Fig. 9. Spatial distribution of information content (IC) and elevation corrected IC (where the median value for each 100 m elevation band is subtracted from the cell IC values), calculated for the monsoon period 2013 (16 June–31 September).

50% of all water sources, whereas half of the total ice melt originates from debris covered areas. Snowmelt represents 37%–47% of annual water inputs in all five subareas defined in Fig. 8b. Table 5 shows that meltwater inputs from regular snow are highest during the pre-monsoon period (March–mid-June), whereas meltwater inputs from avalanched snow peak during the monsoon period. This applies to both the whole basin and to the Lirung subcatchment, and can be explained by heavy snowfalls during the monsoon period in steep areas located at <shigh elevations.

4.5. Information content

The ranking of parameters with highest information content (IC) for annual and seasonal streamflow simulations is provided in Table 6. Parameters that do not exceed the significance level (α) are not shown. Parameter significances are calculated with the Kolmogorov–Smirnov test [85], with α equal to 5%/n, where n is the number of parameters that are included in the analysis (20). The IC-ranks in Table 6 are shown separately for the annual variation in total runoff, the seasonal variations and for the variation in model efficiency (Langtang Khola N&S). For the latter, the 1000 parameter sets are divided into two groups separating parameter sets that lead to higher and lower than median N&S. This is called 'behavioral' partitioning (e.g. [89]). Uncertainty in parameters with a high rank in this category significantly affects the calculated N&S values.

Four parameters (SRF, α_1, T_{mod}, SGR_a) have a high IC in all categories. While SRF, α_1 and T_{mod} have a direct effect on simulated melt (Eq. (2)), SGR_a affects simulated gravitational snow movement. The ranks of the four parameters vary, but SRF has the highest IC for annual and monsoonal streamflow as well as with respect to the behavioral classification. Sub-debris melt parameters that have a significant IC for both annual streamflow volumes and behavioral classification are TF_{d1} (Eq. (4)) and debris thickness (d).

IC-ranks with respect to monsoonal streamflow are almost identical as annual streamflow IC-ranks (Table 6), which means that uncertainty in annual streamflow volumes is mostly determined by the processes that are relevant during the monsoon period. Monsoonal cell-IC is shown in Fig. 9a. Debris covered areas generally have a lower IC than non-debris covered area, whereas IC decreases with debris thickness. Generally, cell IC strongly depends on elevation. The cell IC is highest for non-debris covered glacier area at about 5200 m asl (just below the ELA) such as at Yala Glacier (Fig. 9a). In order to determine which characteristics other than elevation affect cell IC, the basin-wide median cell IC of each 100 m elevation band is subtracted from the cell IC values ('elevation corrected cell IC', Fig. 9b). Elevation corrected cell IC is especially high at the tongues of glaciers in the southwest of the catchment (such as Urkin Kangari or Kanja La), or at Lirung Glacier just above the debris covered area.

Table 1 provides the ranks of glaciers according to the glacier-wide mean cell IC and elevation corrected cell IC. Yala Glacier has the third highest mean cell IC and Lirung Glacier the third highest mean elevation corrected cell IC (Table 1). The highest mean values are calculated in both categories for Urkin Kangari and Kanja La glaciers. We observe that glaciers with a high elevation corrected IC ranks often have a north aspect. An exception is Lirung Glacier which has a south-east aspect. Lirung is by far the steepest glacier in the Langtang catchment (Table 1), which seems to have an effect on model sensitivity and therefore cell-IC. We also calculated the ranks of glaciers with respect to elevation corrected IC for different seasons. The ranks for the monsoon season are nearly identical to those indicated in Table 1. Lirung Glacier has the highest pre-monsoon rank. The highest rank regarding the post-monsoon season is obtained for Kimoshung Glacier. This glacier has a large accumulation area and a low reaching, southward oriented non-debris covered tongue. Temperatures during the post-monsoon period are just high enough that the last 600 m of the tongue (<4700 m asl) are exposed to temperatures above the melting threshold, while for the tongues of other non-debris covered glaciers this is not the case.

5. Discussions

5.1. Model calibration

The calibration approach designed for this study resulted in parameter values that would have been different if no local data had been available for their estimation. This is exemplified by SRF and TF: with only runoff data available for calibration, SRF would be higher and TF lower (Fig. 4a). If SRF and TF had not been calibrated but taken from literature, the chosen parameters would again be different, as the optimal parameter combinations for other high-elevation regions shown in Fig. 4a suggest. Literature values and the calibrated values of TF and SRF indicate that the temperature dependent energy balance components become more important and the shortwave radiation component less important as cloudiness increases (Fig. 4a). The monsoon dominated climate

of the Langtang valley, where the ablation period coincides with the main accumulation period, is different from the climate of other sites where the ETI model has been applied. This study demonstrates thus not only that it is of high importance to use local data for parameter calibration, but also that parameter uncertainty cannot be sufficiently constrained if only one response variable is available for calibration.

The calibration of the snow albedo parameter α_2 also resulted in a high value (0.34, Table 3) previously not reported in literature [75]. α_2 is calibrated against snow albedo measured at AWS Y and a second time against Yala mass balance (MB) observations. There is thus evidence that snow albedo in the Central Himalaya might decrease more rapidly than in other regions. Saturation of snow due to monsoonal rain and dust deposition due to rain-on-snow events may be possible reasons.

While the vast majority of model applications in remote high-elevation catchments use daily time steps, this is to our knowledge the first application of a distributed glacio-hydrological model at an hourly resolution. An advantage of simulating processes with hourly time steps is that the comparison with measured hourly data (e.g. runoff) allows for a more thorough model evaluation. Another advantage is that temperature thresholds have a better physical basis at the hourly resolution. Snow depths measured by a sonic ranging sensor next to the pluviometer at 4831 m asl (Table 2) and air temperature measured at the same location [43] reveals that the mean daily air temperature of days with snowmelt are often well below 0 °C. During hours with above threshold air temperature melt occurs which can be modeled by simulations at hourly resolution but not daily. Other parameters that are affected by the temporal resolution of the simulations are the storage coefficients. Due to the hourly time step, the storage coefficients are conditioned to account for diurnal fluctuations (Fig. 4c). At a coarser time step, these coefficients would be higher to match better the inter-seasonal variability.

Regarding the use of remotely sensed snow cover for model evaluation, Fig. 7 shows the RMSE values of Landsat compared against MODIS snow cover. While Landsat provides high resolution, high quality images of snow cover, the MODIS product is unvalidated in the HKH region and of relatively low spatial resolution. The RMSE calculated between Landsat and MODIS SC can thus be considered as a benchmark for model comparison, since it can be assumed that the error of any model with respect to MODIS cannot be lower than the difference in snow cover between Landsat and MODIS. Landsat vs. MODIS RMSE values are lower by only a few percent than model vs. MODIS RMSE values (Fig. 7), which attests a good performance of the model. However, this questions the utility of MODIS SC for model calibration (such as conducted for the upper Langtang catchment by Konz et al. [49], as in that case the model may be tuned to erroneous observations.

The stepwise scheme for model calibration allowed the identification of knowledge gaps that did not emerge from previous glacio-hydrological model applications in the upper Langtang catchment [11,27,41,42,48,49,72], possibly due to error compensation. The parameters listed in Table 3 were not found to be sufficient to describe the processes at very high elevations (above 5500 m asl) and the precipitation distribution in the east of the catchment. Two additional parameters thus had to be introduced (*CFR* and *PGh2*, Table 4). More precipitation data from the east of the catchment and information about melting conditions above 5500 m asl are required to validate the model setup identified as optimal (Table 4). Measured catchment runoff (Fig. 6a, Table 4) and the annual point mass balance at 5501 m asl (Fig. 4b) suggests that snowmelt from perennial snow refreezes within the snowpack and does thus not contribute to runoff. Snow conditions above 5500 m asl are additionally affected by uncertainty about blowing wind sublimation, a process that can be important at high elevation in the Central Himalaya [90] and that is not considered by the model. Observed Lirung Glacier runoff suggests that the model does not overestimate melt without a parameter *CFR* (and *CFR* was thus only applied to areas outside the Lirung subcatchment). However, an underestimation of precipitation at the flanks of Langtang Lirung peak (7227 m asl), an important orographic barrier, may compensate for an overestimation of meltwater contribution to runoff from above 5500 m asl.

5.2. Simulated water balance and runoff

Snowmelt, rain and ice melt all contribute by at least 26% to the simulated annual water balance (Fig. 8, Table 5). There is a strong seasonal variability in the relative importance of the water balance components: during the hydrological year 2012/2013, snowmelt represented the most important water input to the hydrological system from March to May (84% of all sources) and again in October (57%). In June and in July the hydrology of the catchment was dominated by rainfall (45%) and in August/September by meltwater inputs from ice ablation (47%). Storage changes (derived from changes in soil-, channel-, surface- and englacial reservoir volumes) are the most important contributors to runoff during winter (Table 5). Changes in annual storage between the beginning and the end of the hydrological year are negligible (Fig. 8, Table 5). Racoviteanu et al. [72] have shown that in November 2008 and 2009, an important fraction of channel runoff (30%) had the isotope signature of groundwater. This means that an important fraction of meltwater or rain is routed through the ground. Base flow in winter is reproduced well by the model (Fig. 6a), which suggests that inter-seasonal storage changes are not over- or underestimated or that the soil configuration (Section 3.8) does not need to be revisited. However, the model overestimates catchment runoff during the main monsoon period (Fig. 6a). If the streamflow measurements can be trusted, this overestimation might be due to underestimation of groundwater storage or an underestimation of runoff that is leaving the catchment through the groundwater and not through the channel. Rainfall is an important but also very variable water balance component during this period (Fig. 6b), but the variability in rainfall input to the hydrological system is almost not visible in measured Langtang runoff (Fig. 6a), while some of the variability appears in simulated runoff. It is rather unlikely that the model overestimates rainfall, since precipitation and temperatures are measured at various locations in the valley, and used by the model directly as input data or to estimate meteorological gradients. The effect on streamflow of variable rainfall input to the hydrological system must therefore be buffered by the soil if streamflow data are correct. However, measured monsoon runoff in Himalayan high-elevation catchments must be treated with care. Tracer experiments for the calculation of the rating curve are rarely conducted during the peak monsoon period in July/August, due to difficult road conditions, and the rating curve might therefore not be representative of peak flows. Recorded stage heights may also underestimate peak flows since the radar sensor cannot measure water levels within a very short distance. Peak runoff according to the stage height measurements in 2013 was 17 $m^3 s^{-1}$. The maximum discharge measured by tracer experiments at Langtang Khola on 1 July 2012 was not much below that value (14.95 $m^3 s^{-1}$). However, the tracer experiments were carried out just before intensive monsoon rainfall set in (in total 36.1 mm precipitation measured in Kyangjing on 3 and 4 July 2012). We cannot therefore be sure that the rating curves represent well discharge after intensive monsoon precipitation. Observations by Fukushima et al. [27] show that for the very wet year 1985/1986 (1224.5 mm w.e. precipitation) monsoon mean daily

runoff (measured at a location about 1.3 km upstream of the current gauge) exceeded 30 $m^3 s^{-1}$ every day during July/August. The simulated peak value of 23.8 $m^3 s^{-1}$ of the present study is therefore within the range of observed values. Since the results of all previous glacio-hydrological model applications in the basin [11,27,41,42,48,49,72] are highly sensitive to measured discharge, this highlights the importance of using other in situ data instead of the lumped catchment response for the calibration of model parameters.

5.3. Simulated glacier mass balances

The model simulations of accumulation and ablation resulted in a negative glacier mass balance (−0.24 m w.e. a^{-1}) for the hydrological year 2012/2013, using the model setup that performs best with respect to all available observed data (case 8 in Table 4). Annual mass balances calculated for single glaciers (reported in Table 1) vary between −0.92 m w.e. a^{-1} (Urkin Kangari) and 0.69 m w.e. a^{-1} (Kimoshung). This range of values probably overestimates the actual differences between glaciers. Kimoshung glacier has a large accumulation area that is shielded towards the south by a ridge higher than 6000 m asl. Monsoon clouds moving up-valley may be blocked by that ridge and extrapolated precipitation and therefore mass balance overestimated as a result. Glacier area of Urkin Kangari or of other small, non-debris covered glaciers in the south may be overestimated due to a not up to date glacier mask. The model probably provides more accurate simulations for Yala Glacier, where the monitoring network is dense (Fig. 1). Here, an annual mass balance of −0.17 m w.e. a^{-1} is simulated (Table 1), while the ELA is located at 5400 m asl (Fig. 4b). [22] locate the ELA at Yala Glacier for the periods 1982–96 and 1996–2009 at the same elevation, using GPS and ground-penetrating radar measurements. The ELA in 2011/2012 was slightly higher (5450 m asl, [4], but the year 2013 was characterized by much more post-monsoon precipitation than in 2012. Only 1.3 mm w.e. of precipitation was measured at AWS K in October/November 2012, but 150 mm w.e. during the same period in 2013 due to the cyclone Phailin. Overall, 924.5 mm w.e. precipitation were measured in Kyangjing during the period 18 Nov 2012–17 Nov 2013 which is 284 mm w.e. more than the annual average of the years 1990–2010. This can explain why [88] calculate a mean thinning rate of Yala Glacier for the years 1982–1996 (−0.69 m w.e. a^{-1}) and 1996–2009 (−0.75 m w.e. a^{-1}) that is substantially lower than the modeled mass balance in this study.

The annual mass balances of debris covered glaciers are all negative (Table 1). Melt rates of debris covered areas differ fundamentally from melt rates of bare ice at similar elevations, even when taking into account that supraglacial lakes and cliffs contribute to melt. At 4800 m asl, the annual mean melt rate of bare-ice glacier area is 0.55 m w.e. d^{-1}, whereas the mean melt rate of debris covered area at the same elevation is only 0.07 m w.e. d^{-1}. In comparison to a model run where the presence of supraglacial debris is ignored, melt rates from debris covered glacier area are reduced on average by 84%. Previous studies assumed a reduction of 50% [11] to 70% [42,48] obtained with a constant in time and uniform in space reduction factor.

5.4. Collection of local data

Data collection in 2012 and 2013 at locations on- or near glaciers was concentrated mainly at Lirung and Yala (Fig. 1). Yala was chosen because it is considered as a 'benchmark glacier' for the Himalayan region [22], which has been well investigated in the last 20 years. Lirung Glacier was chosen because of its relatively easy access, previous studies [57,78–80] and because it offered an ideal case to study cliffs and supra-glacial ponds [87]. The information content analysis (Tables 1 and 6 and Fig. 9) allows assessing the effectiveness of ongoing monitoring programs to (i) reduce the uncertainty in model parameters that lead to uncertainty in modeled streamflow, and to (ii) verify that the locations are well chosen in the sense that defining parameter at specific sites effectively leads to less uncertainty in modeled streamflow.

The parameter with the highest information content, *SRF*, was determined by calibration against two different datasets (Lirung streamflow and Yala mass balance). However, the simulations of streamflow and glacier melt are affected by a number of other processes (e.g. temperature distribution, snowfall amounts, albedo, etc.). The model certainly does not represent all these processes perfectly, a fact that may affect the calibrated value of *SRF*. For the design of future field campaigns it would therefore be advisable to install an AWS on bare-ice during the ablation season. Calibration of *SRF* (and *TF*) against the outputs of an energy balance model at the point scale could provide robust parameter estimates (e.g. [73]) that are not affected by potential errors in other model components. AWS Y-G could be used for that purpose, but during the previous field campaign did not measure all the input data necessary to an EB model (e.g. wind speed) due to technical problems. Fresh snow albedo (α_1) is the parameter with the second highest ranks in Table 6 and was determined using the observed snow albedo of 12 snowfall events at AWS Y (Table 3). Since AWS Y is a permanent weather station, future data can be used for a more complete statistical analysis. SGR_a seems to be an important parameter (Table 6). For safety reasons it is not advisable to measure snow depths in avalanche areas; the function that relates snow holding depth to slope will therefore always have to be determined by indirect methods such as by calibration against remotely sensed avalanche patterns, as in this study. Finally, to limit the discussion to the parameters that are among the top five in annual IC in Table 6, T_{mod} and T_T are temperature related parameters which in theory can be directly determined with the current monitoring setup. However, those are parameters whose uncertainty is naturally high. T_{mod} is associated with the variability of air temperature over glacierized surfaces, which is high especially during the day, poorly understood and controlled by katabatic flows and energy fluxes in the glacier boundary layer. T_T is an empirical parameters that is normally assumed or calibrated, but depends also on meteorological conditions, the energy balance at the glacier surface and on the cold content of the snow pack. Given this, it is unrealistic to determine a single optimal value for T_{mod} and T_T. It is therefore recommended to vary these parameters following a Monte Carlo procedure to provide robust projections of simulated streamflow.

Regarding the choice of the locations for fieldwork, the results of the information content analysis are encouraging. Yala Glacier has the third highest mean IC and Lirung Glacier the third highest IC if elevation effects are omitted (Table 1). In the case of Yala Glacier the model is sensitive to the transition from a snow covered to an ice exposed surface, which due to changes in albedo leads to strong variations in simulated melt. Field campaigns in the region should therefore always focus on elevations above and below the potential location of the ELA. If the approximate elevation of the ELA is known, this value should be used as a response variable for model calibration. For the present study, the ablation stakes confirmed that the model reproduces the ELA correctly at Yala Glacier. Regarding Lirung Glacier, the fieldwork was concentrated on the tongue, while it is the steep area above the glacier cirque that has a high information content. Fieldwork on the tongue is necessary to fill the data gap which exists about processes on debris covered glaciers. However, measured glacier runoff allowed the uncertainty in modeled meltwater contribution from higher elevations to also be constrained. Avalanching is an important process on Lirung (Fig. 8), and remotely sensed avalanche patterns were therefore evaluated at a very relevant location.

The high IC of Urkin Kangari and Kanja La glaciers does not mean that the monitoring program needs to be entirely transferred to the southern side of the basin, since glaciers there are relatively small. The sum of all cell IC of all glacier area in the south-west of the catchment is still less than the sum of all cell IC calculated for Langtang Glacier only. However, temperature and precipitation data and an updated glacier map would be beneficial in order to assess if the model represents the glacio-meteorological conditions correctly in the south-west.

6. Conclusions

New detailed in situ data from the upper Langtang catchment, the core study catchment of various institutions doing research in the Central Himalaya, are used to set up a state-of-the-art glacio-hydrological model and provide a fundamental understanding of the complex hydrology of this Himalayan catchment. The model is used to quantify processes that have been previously suggested to be important in Himalayan catchments but never quantified before. We use it to provide estimates of the contribution of glaciers and snow to catchment runoff and their spatial and temporal variability.

14 parameters are directly calculated on the basis of local data, and 13 parameters are calibrated against 5 different datasets (Table 3, Fig. 2). Measured catchment runoff and remotely sensed snow cover – datasets that are used in previous modeling studies in the region to tune model parameters but in high-elevation regions are often affected by significant uncertainties – are not used for model calibration but only for validation. All parameter values derived in this study can be directly linked to physical processes that can be observed. The methodology to derive various parameter values can be regarded as a benchmark for future efforts to calibrate glacio-hydrological models. However, the systematic approach to estimate model parameters based on local data also revealed further data gaps, not often discussed in literature, that are significantly affecting the performance of glacio-hydrological models. As such, there remains uncertainty about snowmelt contribution to runoff from perennial snow (>5500 m asl) and about the spatial variability of precipitation. However, by employing all 27 model parameters that are included in the calibration scheme, and by making realistic assumptions about the spatial variability of precipitation and melt at high elevations, the model is capable of reproducing observed catchment runoff and snow cover accurately.

The systematic integration of detailed local information on physical processes enhances the capacity of the model to unravel the full water balance of the study catchment. Snowmelt is the most important contributor to total runoff during the hydrological year 2012/2013 (representing 40% of all sources), followed by rainfall (34%) and ice melt (26%). From March to May and again in October snowmelt represented the most important streamflow source. In June and in July the hydrology of the catchment was dominated by rainfall and in August/September by meltwater inputs from ice ablation. Note that these results might differ slightly for years with considerably different meteorological conditions than during the hydrological year 2012/2013.

A novel approach is used to generate maps of spatially varying debris thickness. The role of supraglacial lakes and cliffs on the total melt of a debris covered glacier is indirectly taken into account by attributing more shallow debris to model grid cells that contain lakes and cliffs. In combination with a new sub-debris melt model, we provide the first estimation of the melt reducing effect of supraglacial debris in the upper Langtang catchment that is based on in situ data. We find that melt rates on average are reduced by 84%, which is more than assumed by previous modeling studies [11,42,48]. In spite of the lower melt rates below debris, simulated annual glacier mass balances of debris covered glaciers are of similar magnitude than those of non debris covered glaciers. Overall, the mass balance of glacierized area of the upper Langtang catchment for the hydrological year 2012/2013 was −0.24 m w.e. One third of total ice melt originated from the debris covered glacier parts.

The analysis of the spatial distribution of information content confirms the effectiveness of the current monitoring setup, since the installed network is concentrated at locations where the uncertainty in glacier mass balance due to uncertainty in model parameters significantly affects uncertainty in simulated catchment runoff. The analysis underlines that it is fundamental for the performance of a glacio-hydrological model to represent well the ELA, as previous studies have concluded (e.g. [72]). The information content analysis also reveals that a significant portion of runoff uncertainty can be attributed to uncertainty in modeling gravitational snow redistribution, although only about 5% of total water inputs to the hydrological system originate from melted snow that had been moved by avalanches. Since avalanching can have locally and temporarily an important effect on the water balance, this processes need to be considered by glacio-hydrological models in the Central Himalaya. With respect to potential applications of the model for future projections, an effort should be made to collect the relevant data to integrate melt from supraglacial cliffs and lakes explicitly into the model, in order to further improve its predictive skills.

Acknowledgments

This study was part of the HKH Cryosphere Monitoring Project (CMP) implemented by the International Centre for Integrated Mountain Development and supported by the Norwegian Ministry of Foreign Affairs. The authors would like to thank the CMP project partners for their help in carrying out this study, including the Himalayan Cryosphere, Climate and Disaster Research Center, Kathmandu University; Central Department of Hydrology and Meteorology, Tribhuvan University; Department of Hydrology and Meteorology, Government of Nepal; and Water and Energy Commission Secretariat, Government of Nepal. This study was partially funded by the USAID High Mountain Glacier Watershed Programs Climber-Scientist (Grant No. CCRDCS0010), which is warmly acknowledge for its support, and by the South Asia Research Hub of the UK Department for International Development (DFID). Stefan Rimkus did all the necessary modifications in the code of TOP-KAPI-ETH and Anna Chesnokova and Simon Wicki helped with the energy balance modeling of Lirung Glacier which is gratefully acknowledged. The authors would like to thank very much all the people that contributed to the data collection. The authors are grateful to Koji Fujita and two anonymous reviewers for providing thoughtful and useful reviews. Special thanks go to Paolo Burlando for supporting Silvan Ragettli's work at ETH.

References

[1] Ageta Y, Iida H, Watanabe O. Glaciological studies on Yala Glacier in Langtang Himal, Glacial Studies in Langtang Valley, Report of the Boring Project 1981–82 in the Nepal Himalaya, 2, 41–47; 1984.
[2] Anderton S, Latron J, Gallart F. Sensitivity analysis and multi-response, multi-criteria evaluation of a physically based distributed model. Hydrol Processes 2002;16(2):333–53. http://dx.doi.org/10.1002/hyp.336.
[3] Bajracharya SR, Shrestha B. The status of glaciers in the Hindu Kush-Himalayan Region. Kathmandu, Nepal: ICIMOD; 2011.
[4] Baral P et al. Preliminary results of mass-balance observations of Yala Glacier and analysis of temperature and precipitation gradients in Langtang Valley, Nepal. Ann Glaciol 2014;55(66):9–14. http://dx.doi.org/10.3189/2014AoG66A106.

[5] Bárdossy a, Singh SK. Robust estimation of hydrological model parameters. Hydrol Earth Syst Sci 2008;12(6):1273–83. http://dx.doi.org/10.5194/hess-12-1273-2008.

[6] Benn D et al. Response of debris-covered glaciers in the Mount Everest region to recent warming, and implications for outburst flood hazards. Earth-Sci Rev 2012;114(1–2):156–74. http://dx.doi.org/10.1016/j.earscirev.2012.03.008.

[7] Bernhardt M, Schulz K. SnowSlide: a simple routine for calculating gravitational snow transport. Geophys Res Lett 2010;37(11):L11502. http://dx.doi.org/10.1029/2010GL043086.

[8] Beven K. Uniqueness of place and process representations in hydrological modelling. Hydrol Earth Syst Sci 2000;4(2):203–13. http://dx.doi.org/10.5194/hess-4-203-2000.

[9] Bocchiola D, Diolaiuti G, Soncini a, Mihalcea C, D'Agata C, Mayer C, Lambrecht a, Rosso R, Smiraglia C. Prediction of future hydrological regimes in poorly gauged high altitude basins: the case study of the upper Indus, Pakistan. Hydrol Earth Syst Sci 2011;15(7):2059–75. http://dx.doi.org/10.5194/hess-15-2059-2011.

[10] Bolch T et al. The state and fate of Himalayan glaciers. Science 2012;336(6079):310–4. http://dx.doi.org/10.1126/science.1215828.

[11] Braun L, Grabs W, Rana B. Application of a conceptual precipitation-runoff model in the Langtang Khola Basin, Nepal Himalaya. IAHS Publ 1993;218:221–37.

[12] Brock B, Willis I, Sharp M. Measurement and parameterization of albedo variations at Haut Glacier d'Arolla, Switzerland. J Glaciol 2000;46:675–88. http://dx.doi.org/10.3189/172756500781832675.

[13] Brock BW, Mihalcea C, Kirkbride MP, Diolaiuti G, Cutler MEJ, Smiraglia C. Meteorology and surface energy fluxes in the 2005–2007 ablation seasons at the Miage debris-covered glacier, Mont Blanc Massif, Italian Alps. J Geophys Res 2010;115(D09106). http://dx.doi.org/10.1029/2009JD013224.

[14] Carenzo M, Pellicciotti F, Rimkus S, Burlando P. Assessing the transferability and robustness of an enhanced temperature-index glacier-melt model. J Glaciol 2009;55(190):258–74. http://dx.doi.org/10.3189/002214309788608804.

[15] Carenzo M, Pellicciotti F, Mabillard J, Reid T, Brock BW. An enhanced debris temperature index model accounting for thickness effect. Adv Water Resour (in preparation). 2015.

[16] Cogley JG. Himalayan glaciers in the balance. Nature 2012;488(7412):468–9. http://dx.doi.org/10.1038/488468a.

[17] Corripio J. Vectorial algebra algorithms for calculating terrain parameters from DEMs and solar radiation modelling in mountainous terrain. Int J Geog Inf Sci 2003;17(1):1–23. http://dx.doi.org/10.1080/713811744.

[18] Fatichi S, Rimkus S, Burlando P, Bordoy R. Does internal climate variability overwhelm climate change signals in streamflow? The upper Po and Rhone basin case studies. Sci Total Environ 2014;493:1171–82. http://dx.doi.org/10.1016/j.scitotenv.2013.12.014.

[19] Finger D, Pellicciotti F, Konz M, Rimkus S, Burlando P. The value of glacier mass balance, satellite snow cover images, and hourly discharge for improving the performance of a physically based distributed hydrological model. Water Resour Res 2011;47(7):1–14. http://dx.doi.org/10.1029/2010WR009824.

[20] Finger D, Heinrich G, Gobiet A, Bauder A. Projections of future water resources and their uncertainty in a glacierized catchment in the Swiss Alps and the subsequent effects on hydropower production during the 21st century. Water Resour Res 2012;48(2):1–20. http://dx.doi.org/10.1029/2011WR010733.

[21] Foster LA, Brock BW, Cutler MEJ, Diotri F. A physically based method for estimating supraglacial debris thickness from thermal band remote-sensing data. J Glaciol 2012;58(210):677–91. http://dx.doi.org/10.3189/2012JoG11J194.

[22] Fujita K, Nuimura T. Spatially heterogeneous wastage of Himalayan glaciers. Proc Nat Acad Sci USA 2011;108(34):14011–4. http://dx.doi.org/10.1073/pnas.1106242108.

[23] Fujita K, Sakai a. Modelling runoff from a Himalayan debris-covered glacier. Hydrol Earth Syst Sci 2014;18(7):2679–94. http://dx.doi.org/10.5194/hess-18-2679-2014.

[24] Fujita K, Takeuchi N, Seko K. Glaciological observations of Yala Glacier in Langtang Valley, Nepal Himalayas, 1994 and 1996. Bull Glacier Res 1998;16:75–81.

[25] Fujita K, Thompson LG, Ageta Y, Yasunari T, Kajikawa Y, Sakai A, Takeuchi N. Thirty-year history of glacier melting in the Nepal Himalayas. J Geophys Res 2006;111(D03109):1–6. http://dx.doi.org/10.1029/2005JD005894.

[26] Fujita K, Suzuki R, Nuimura T, Sakai A. Performance of ASTER and SRTM DEMs, and their potential for assessing glacial lakes in the Lunana region, Bhutan Himalaya. J Glaciol 2008;54(185):220–8. http://dx.doi.org/10.3189/002214308784886162.

[27] Fukushima Y, Watanabe O, Higuchi K. Estimation of streamflow change by global warming in a glacier-covered high mountain area of the Nepal Himalaya. IAHS Publ 1991;205:181–8.

[28] Gabbi J, Carenzo M, Pellicciotti F, Bauder A, Funk M. A comparison of empirical and physically-based glacier surface melt models for long-term simulations of glacier response. J Glaciol 2014;60(224):1140–54. http://dx.doi.org/10.3189/2014JoG14J011.

[29] Gardelle J, Berthier E, Arnaud Y, Kääb A. Region-wide glacier mass balances over the Pamir-Karakoram-Himalaya during 1999–2011. Cryosphere 2013;7(4):1263–86. http://dx.doi.org/10.5194/tc-7-1263-2013.

[30] Hall D, Riggs G. Accuracy assessment of the MODIS snow products. Hydrol Processes 2007;1547:1534–47. http://dx.doi.org/10.1002/hyp.

[31] Hall DK, Riggs Ga, Salomonson VV, DiGirolamo NE, Bayr KJ. MODIS snow-cover products. Remote Sensing Environ 2002;83(1–2):181–94. http://dx.doi.org/10.1016/S0034-4257(02)00095-0.

[32] Hannah DM, Gurnell AM. A conceptual, linear reservoir runoff model to investigate melt season changes in cirque glacier hydrology. J Hydrol 2001;246(1–4):123–41. http://dx.doi.org/10.1016/S0022-1694(01)00364-X.

[33] Hewitt K. The Karakoram anomaly? Glacier expansion and the 'elevation effect', Karakoram Himalaya. Mt Res Dev 2005;25(4):332–40. http://dx.doi.org/10.1659/0276-4741(2005)0250332:TKAGEA2.0.CO;2.

[34] Hewitt K. Glacier change concentration, and elevation effects in the Karakoram Himalaya, Upper Indus Basin. Mt Res Dev 2011;31(3):188–200. http://dx.doi.org/10.1659/MRD-JOURNAL-D-11-00020.1.

[35] Hornberger GM, Spear RC. An approach to the preliminary analysis of environmental systems. J Environ Manage 1981;12(1):7–18.

[36] Huss M, Farinotti D. Distributed ice thickness and volume of all glaciers around the globe. J Geophys Res 2012;117(F4):F04010. http://dx.doi.org/10.1029/2012JF002523.

[37] Huss M, Zemp M, Joerg PC, Salzmann N. High uncertainty in 21st century runoff projections from glacierized basins. J Hydrol 2014;510:35–48. http://dx.doi.org/10.1016/j.jhydrol.2013.12.017.

[38] Iida H, Watanabe O, Mulmi D, Thapa K. Glacier distribution in the Langtang river region, Nepal, Glacial Studies in Langtang Valley. Report of the Boring Project 1981–82 in the Nepal Himalaya: 2; 1984. p. 117–20.

[39] Immerzeel W, Van Beek L, Bierkens M. Climate change will affect the Asian water towers. Science 2010;328(5984):1382–5. http://dx.doi.org/10.1126/science.1183188.

[40] Immerzeel W, Kraaijenbrink P, Shea J, Shrestha AB, Pellicciotti F, Bierkens M, de Jong S. High-resolution monitoring of Himalayan glacier dynamics using unmanned aerial vehicles. Remote Sensing Environ 2014;150:93–103. http://dx.doi.org/10.1016/j.rse.2014.04.025a.

[41] Immerzeel WW, Beek LPH, Konz M, Shrestha AB, Bierkens MFP. Hydrological response to climate change in a glacierized catchment in the Himalayas. Clim Change 2012;110:721–36. http://dx.doi.org/10.1007/s10584-011-0143-4.

[42] Immerzeel WW, Pellicciotti F, Bierkens MFP. Rising river flows throughout the twenty-first century in two Himalayan glacierized watersheds. Nat Geosci 2013;6(8):1–4. http://dx.doi.org/10.1038/ngeo1896.

[43] Immerzeel WW, Petersen L, Ragettli S, Pellicciotti F. The importance of observed gradients of air temperature and precipitation for modeling runoff from a glacierized watershed in the Nepalese Himalayas. Water Resour Res 2014;50:1–15. http://dx.doi.org/10.1002/2013WR014506b.

[44] Iqbal M. An introduction to solar radiation. London: Academic Press; 1983. 390 p.

[45] Jansson P, Hock R, Schneider T. The concept of glacier storage: a review. J Hydrol 2003;282(1–4):116–29. http://dx.doi.org/10.1016/S0022-1694(03)00258-0.

[46] Kääb A, Berthier E, Nuth C, Gardelle J, Arnaud Y. Contrasting patterns of early twenty-first-century glacier mass change in the Himalayas. Nature 2012;488(7412):495–8. http://dx.doi.org/10.1038/nature11324.

[47] Kirkbride MP, Deline P. The formation of supraglacial debris covers by primary dispersal from transverse englacial debris bands. Earth Surf Processes Landforms 2013;38(15):1779–92. http://dx.doi.org/10.1002/esp.3416.

[48] Konz M, Uhlenbrook S, Braun L. Implementation of a process-based catchment model in a poorly gauged, highly glacierized Himalayan headwater. Hydrol Earth Syst Sci 2007;11:1323–39. http://dx.doi.org/10.5194/hess-11-1323-2007.

[49] Konz M, Finger D, Bürgi C, Normand S, Immerzeel WW. Calibration of a distributed hydrological model for simulations of remote glacierized Himalayan catchments using MODIS snow cover data. IAHS Publ 2010;340:465–73.

[50] Kotchenova SY, Vermote EF, Matarrese R, Klemm FJ. Validation of a vector version of the 6S radiative transfer code for atmospheric correction of satellite data. Part I: path radiance. Appl Opt 2006;45(26):6762–74. http://dx.doi.org/10.1364/AO.45.006762.

[51] Liu Z, Todini E. Towards a comprehensive physically-based rainfall-runoff model. Hydrol Earth Syst Sci 2002;6:859–81. http://dx.doi.org/10.5194/hess-6-859-2002.

[52] Liu Z, Todini E. Assessing the TOPKAPI non-linear reservoir cascade approximation by means of a characteristic lines solution. Hydrol Processes 2005;19(10):1983–2006. http://dx.doi.org/10.1002/hyp.5662.

[53] Lutz A, Immerzeel W, Shrestha A, Bierkens M. Consistent increase in High Asia's runoff due to increasing glacier melt and precipitation. Nat Clim Change 2014;4:587–92. http://dx.doi.org/10.1038/NCLIMATE2237.

[54] Mabillard J. Distributed modelling of changes in glacier mass balance and runoff on Miage glacier [Master thesis]. Italy: Institute of Environmental Engineering, ETH–Zurich; 2012.

[55] Mihalcea C, Mayer C, Diolaiuti G, Lambrecht A, Smiraglia C, Tartari G. Ice ablation and meteorological conditions on the debris-covered area of Baltoro glacier, Karakoram, Pakistan. Ann Glaciol 2006;43(1):292–300. http://dx.doi.org/10.3189/172756406781812104.

[56] Mukhopadhyay B. Detection of dual effects of degradation of perennial snow and ice covers on the hydrologic regime of a Himalayan river basin by stream water availability modeling. J Hydrol 2012;412–413:14–33. http://dx.doi.org/10.1016/j.jhydrol.2011.06.005.

[57] Naito N, Nakawo M, Aoki T, Asahi K, Fujita K, Sakai A, et al. Surface flow on the ablation area of the Lirung Glacier in Langtang Valley, Nepal Himalayas. Bull Glacier Res 1998;16:67–73.

[58] Nash JE, Sutcliffe JV. River flow forecasting through conceptual models. Part I–A discussion of principles. J Hydrol 1970;10(3):282–90. http://dx.doi.org/10.1016/0022-1694(70)90255-6.

[59] Nepal S, Krause P, Flügel W-A, Fink M, Fischer C. Understanding the hydrological system dynamics of a glaciated alpine catchment in the Himalayan region using the J2000 hydrological model. Hydrol Processes 2013;28:1329–44. http://dx.doi.org/10.1002/hyp.9627.

[60] Nuimura T, Fujita K, Yamaguchi S, Sharma RR. Elevation changes of glaciers revealed by multitemporal digital elevation models calibrated by GPS survey in the Khumbu region, Nepal Himalaya, 1992–2008. J Glaciol 2012;58(210):648–56. http://dx.doi.org/10.3189/2012JoG11J061.

[61] Nuimura T et al. The GAMDAM glacier inventory: a quality controlled inventory of Asian glaciers. Cryosphere Discuss 2014;8(3):2799–829. http://dx.doi.org/10.5194/tcd-8-2799-2014.

[62] Østrem G. Ice melting under a thin layer of moraine, and the existence of ice cores in moraine ridges. Geografiska Annaler 1959;41(4):228–30.

[63] Paul F, Huggel C, Kääb A. Combining satellite multispectral image data and a digital elevation model for mapping debris-covered glaciers. Remote Sensing Environ 2004;89(4):510–8. http://dx.doi.org/10.1016/j.rse.2003.11.007.

[64] Pellicciotti F, Brock B, Strasser U, Burlando P, Funk M, Corripio J. An enhanced temperature-index glacier melt model including the shortwave radiation balance: development and testing for Haut Glacier d Arolla, Switzerland. J Glaciol 2005;51(175):573–87. http://dx.doi.org/10.3189/172756505781829124.

[65] Pellicciotti F, Helbing J, Rivera A, Favier V, Corripio J, Araos J, et al. A study of the energy balance and melt regime on Juncal Norte Glacier, semi-arid Andes of central Chile, using melt models of different complexity. Hydrol Processes 2008;22:3980–97. http://dx.doi.org/10.1002/hyp.7085.

[66] Pellicciotti F, Buergi C, Immerzeel WW, Konz M, Shrestha AB. Challenges and uncertainties in hydrological modeling of remote Hindu Kush-Karakoram-Himalayan (HKH) basins: suggestions for calibration strategies. Mt Res Dev 2012;32(1):39–50. http://dx.doi.org/10.1659/MRD-JOURNAL-D-11-00092.1.

[67] Pellicciotti F, Ragettli S, Carenzo M, McPhee J. Changes of glaciers in the Andes of Chile and priorities for future work. Sci Total Environ 2014;493:1197–210. http://dx.doi.org/10.1016/j.scitotenv.2013.10.055.

[68] Pellicciotti F, Stephan C, Miles E, Immerzeel WW, Bolch T. Mass balance changes of debris-covered glaciers in the Langtang Himal in Nepal between 1974 and 1999. J Glaciol 2015;61(225):1–14. http://dx.doi.org/10.3189/2015JoG13J237.

[69] Petersen L, Schauwecker S, Brock B, Immerzeel W, Pellicciotti F. Deriving supraglacial debris thickness using satellite data on the Lirung Glacier in the Nepalese Himalayas. Geophys Res Abstr 2013;15(10):244.

[70] Prasch M, Mauser W, Weber M. Quantifying present and future glacier melt-water contribution to runoff in a central Himalayan river basin. Cryosphere 2013;7(3):889–904. http://dx.doi.org/10.5194/tc-7-889-2013.

[71] Priestley C, Taylor R. On the assessment of surface heat flux and evaporation using large-scale parameters. Mon Weather Rev 1972;100(2):81–92. http://dx.doi.org/10.1175/1520-0493(1972)100<0081:OTAOSH 2.3.CO;2.

[72] Racoviteanu AE, Armstrong R, Williams MW. Evaluation of an ice ablation model to estimate the contribution of melting glacier ice to annual discharge in the Nepal Himalaya. Water Resour Res 2013;49(9):5117–33. http://dx.doi.org/10.1002/wrcr.20370.

[73] Ragettli S, Pellicciotti F. Calibration of a physically based, spatially distributed hydrological model in a glacierized basin: on the use of knowledge from glaciometeorological processes to constrain model parameters. Water Resour Res 2012;48(3):1–20. http://dx.doi.org/10.1029/2011WR010559.

[74] Ragettli S, Cortez G, McPhee J, Pellicciotti F. An evaluation of approaches for modeling hydrological processes in high-elevation, glacierized Andean watersheds. Hydrol Processes 2013;28(23):5674–95. http://dx.doi.org/10.1002/hyp.10055a.

[75] Ragettli S, Pellicciotti F, Bordoy R, Immerzeel W. Sources of uncertainty in modeling the glaciohydrological response of a Karakoram watershed to climate change. Water Resour Res 2013;49(9):6048–66. http://dx.doi.org/10.1002/wrcr.20450b.

[76] Reid TD, Brock BW. An energy-balance model for debris-covered glaciers including heat conduction through the debris layer. J Glaciol 2010;56(199):903–16. http://dx.doi.org/10.3189/002214310794457218.

[77] Rohrer M, Salzmann N, Stoffel M, Kulkarni AV. Missing (in-situ) snow cover data hampers climate change and runoff studies in the Greater Himalayas. Sci Total Environ 2013;468–469(Supplement S60–S70). http://dx.doi.org/10.1016/j.scitotenv.2013.09.056.

[78] Sakai A, Nakawo M, Fujita K. Melt rate of ice cliffs on the Lirung Glacier, Nepal Himalayas, 1996. Bull Glacier Res 1998;16:57–66.

[79] Sakai A, Takeuchi N, Fujita K, Nakawo M. Role of supraglacial ponds in the ablation process of a debris-covered glacier in the Nepal Himalayas. IAHS Publ 2000;265:119–30.

[80] Sakai A, Nakawo M, Fujita K. Distribution characteristics and energy balance of ice cliffs on debris-covered glaciers, Nepal Himalaya. Arctic Antarctic Alpine Res 2002;34(1):12–9. http://dx.doi.org/10.2307/1552503.

[81] Sakai A, Fujita K, Kubota J. Evaporation and percolation effect on melting at debris-covered Lirung Glacier, Nepal Himalayas, 1996. Bull Glaciol Res 2004;21:9–15.

[82] Saxton KE, Rawls WJ. Soil water characteristic estimates by texture and organic matter for hydrologic solutions. Soil Sci Soc Am J 2006;70(5):1569–78. http://dx.doi.org/10.2136/sssaj2005.0117.

[83] Shangguan D et al. Glacier changes in the Koshi River basin, central Himalaya, from 1976 to 2009, derived from remote-sensing imagery. Ann Glaciol 2014;55(66):61–8. http://dx.doi.org/10.3189/2014AoG66A057.

[84] Shiraiwa T, Ueno K, Yamada T. Distribution of mass input on glaciers in the Langtang Valley, Nepal Himalayas. Bull Glacier Res 1992;10:21–30.

[85] Spear RC, Hornberger GM. Eutrophication in peel inlet. 2. Identification of critical uncertainties via generalized analysis. Water Res 1980;14(1):43–9. http://dx.doi.org/10.1016/0043-1354(80)90040-8.

[86] Steinegger U, Braun L, Kappenberger G, Tartari G. Assessment of annual snow accumulation over the past 10 years at high elevations in the Langtang region. IAHS Publ 1993;218:155–66.

[87] Steiner JF, Pellicciotti F, Buri P, Evan S, Immerzeel WW. Modeling ice cliff backwasting on a debris covered glacier in the Nepalese Himalayas. J Glaciol. 2014: p. 1–17 (under review).

[88] Sugiyama S, Fukui K, Fujita K, Tone K, Yamaguchi S. Changes in ice thickness and flow velocity of Yala Glacier, Langtang Himal, Nepal, from 1982 to 2009. Ann Glaciol 2013;54(64):157–62. http://dx.doi.org/10.3189/2013AoG64A111.

[89] Tang Y, Reed P, Wagener T, van Werkhoven K. Comparing sensitivity analysis methods to advance lumped watershed model identification and evaluation. Hydrol Earth Syst Sci 2007;11(2):793–817. http://dx.doi.org/10.5194/hess-11-793-2007.

[90] Wagnon P et al. Seasonal and annual mass balances of Mera and Pokalde glaciers (Nepal Himalaya) since 2007. Cryosphere 2013;7(6):1769–86. http://dx.doi.org/10.5194/tc-7-1769-2013.

[91] Wang X, Xie H, Liang T. Evaluation of MODIS snow cover and cloud mask and its application in Northern Xinjiang, China. Remote Sensing Environ 2008;112(4):1497–513. http://dx.doi.org/10.1016/j.rse.2007.05.016.

[92] Wicki S. Energy balance modelling over the debris-covered Lirung Glacier [Master thesis]. Nepalese Himalaya: Department of Environmental Engineering, ETH Zurich; 2014.

[93] Yao T et al. Different glacier status with atmospheric circulations in Tibetan Plateau and surroundings. Nat Clim Change 2012;2(9):663–7. http://dx.doi.org/10.1038/nclimate1580.

[94] Zelazowski P, Sayer AM, Thomas GE, Grainger RG. Reconciling satellite-derived atmospheric properties with fine-resolution land imagery: insights for atmospheric correction. J Geophys Res 2011;116(D18308):1–15. http://dx.doi.org/10.1029/2010JD015488.

[95] Zhang Y, Fujita K, Liu S, Liu Q, Nuimura T. Distribution of debris thickness and its effect on ice melt at Hailuogou glacier, southeastern Tibetan Plateau, using in situ surveys and ASTER imagery. J Glaciol 2011;57(206):1147–57. http://dx.doi.org/10.3189/002214311798843331.